Measurement report: The importance of biomass burning in light extinction and direct radiative effect of urban aerosol during the COVID-19 lockdown in Xi'an, China

Jie Tian[1,2], Qiyuan Wang[1,2,3], Huikun Liu[1], Yongyong Ma[4], Suixin Liu[1,2], Yong Zhang[1], Weikang Ran[1], Yongming Han[1,2,3], and Junji Cao[5]

[1]State Key Laboratory of Loess and Quaternary Geology, Institute of Earth Environment, Chinese Academy of Sciences, Xi'an 710061, China
[2]CAS Center for Excellence in Quaternary Science and Global Change, Xi'an 710061, China
[3]National Observation and Research Station of Regional Ecological Environment Change and Comprehensive Management in the Guanzhong Plain, Shaanxi, Xi'an 710061, China
[4]Meteorological Institute of Shaanxi Province, Xi'an 710015, China
[5]Institute of Atmospheric Physics, Chinese Academy of Sciences, Beijing 100029, China

Correspondence: Qiyuan Wang (wangqy@ieecas.cn) and Junji Cao (jjcao@mail.iap.ac.cn)

Abstract. Due to the complexity of emission sources, a better understanding of aerosol optical properties is required to mitigate climate change in China. Here, an intensive real-time measurement was conducted in an urban area of China before and during the lockdown of Coronavirus Disease 2019 (COVID-19), to explore the impacts of anthropogenic activities on aerosol light extinction and direct radiative effect (DRE). The mean light extinction coefficient (b_{ext}) reduced from 774.7 $\pm$298.1 Mm^{-1} during the normal period to 544.3 $\pm$179.4 Mm^{-1} during the lockdown period. The generalized additive model analysis indicated that the large decline of b_{ext} (29.7%) was attributed to the sharp reductions in anthropogenic emissions. Chemical calculation of b_{ext} based on the ridge regression analysis showed that organic aerosol (OA) was the largest contributor to b_{ext} in both periods (45.1–61.4%), and contributions of two oxygenated OAs to b_{ext} increased by 3.0–14.6% during the lockdown. A hybrid environmental receptor model combining with chemical and optical variables identified six sources of b_{ext}. It was found that b_{ext} from traffic-related emission, coal combustion, fugitive dust, nitrate plus secondary OA (SOA) source, and sulfate plus SOA source decreased by 21.4–97.9% in the lockdown, whereas b_{ext} from biomass burning increased by 27.1% mainly driven by undiminished needs of residential cooking and heating. The atmospheric radiative transfer model was further used to illustrate that biomass burning instead of traffic-related emission became the largest positive effect (10.0 $\pm$ 10.9 W m^{-2}) on aerosol DRE in the atmosphere during the lockdown. Our study provides insights into aerosol b_{ext} and DRE from anthropogenic sources, and the results implied the importance of controlling biomass burning for tackling climate change in China in the future.

1 Introduction

The abrupt outbreak of Coronavirus Disease 2019 (COVID-19) caused unprecedented economic and social disruption (Yao et al., 2020). Most worldwide countries implemented the city lockdown to curb the virus spread among humans, providing a rare opportunity to investigate the impacts of anthropogenic activities on the air quality (Ibrahim et al., 2021; Kumar et al., 2021; Sanap, 2021; Weber et al., 2020). The Chinese government also enforced a series of strict restrictions on travel, transport, manufacture, and constructive activities during the lockdown. Recent studies on the aerosols in China which were conducted during the lockdown period focused on primary emissions and secondary formation, and most of them had revealed changes in aerosol compositions, sources, and processes under a variety of emission control measures (Le et al., 2020; Li et al., 2020; Wang et al., 2020a; Wang et al., 2020c; Zhao et al., 2020; Zheng et al., 2020). However, only a few studies were conducted to explore the link of chemical constituents in aerosol with light absorption during the lockdown (Chen et al., 2020; Lin et al., 2021; Xu et al., 2020a). The influences of reduced anthropogenic activities on the variations of aerosol optical properties and direct radiative effect (DRE) are less understood.

Atmospheric aerosols alter the radiative energy budget by directly scattering and absorbing solar and terrestrial radiation to affect global climate change (Bellouin et al., 2013; Yao et al., 2017). The spatiotemporal variations of aerosol optical properties (e.g., light scattering coefficient (b_{scat}), light absorption coefficient (b_{abs}), light extinction coefficient (b_{ext}), and single scattering albedo (SSA)) highly depended on their chemical compositions and sources (Malm and Hand, 2007; Tao et al., 2014; Yao et al., 2021), can elevate uncertainties in estimating aerosol DRE (IPCC, 2013; Ma et al., 2012). Therefore, distinguishing chemical composition- and source-specific aerosol optical properties from a mixture of aerosols in the atmosphere would make a better understanding of the climate change during the COVID-19 lockdown.

The relationship between aerosol optical coefficients and chemical compositions can be built by the Interagency Monitoring of Protected Visual Environments algorithm and multiple linear regression (MLR) (Deng et al., 2016; Malm and Hand, 2007; Shen et al., 2014; Tao et al., 2014, 2015). However, previous studies often regarded organic aerosol (OA) as a whole light scattering component only. In reality, some OA components can absorb light, which is collectively termed as brown carbon (BrC) (Andreae and Gelencsér, 2006). The DRE caused by BrC has been reported to be nonnegligible (e.g., 0.04 W m^{-2} to 0.57 W m^{-2}) (Feng et al., 2013; Lin et al., 2014; Wang et al., 2014). Furthermore, the optical properties of OA can vary widely due to the complexity of OA components associated with primary sources, formation pathways, and aging processes (Laskin et al., 2015). For instance, primary OA (POA) from anthropogenic sources (e.g., biomass burning and coal combustion) usually has different mass scattering and absorption efficiencies (MSE and MAE) in the atmosphere compared to secondary OA (SOA) formed though photochemical or aqueous-phase oxidations (Han et al., 2015; Qin et al., 2018). Therefore, investigating POA and SOA contributions to aerosol light scattering and absorption would reduce uncertainties in the chemical apportionment of aerosol optical properties.

Previous studies have been conducted on the aerosol optical source apportionment. According to the multi-wavelength aethalometer measurement, the source of aerosol b_{abs} can be investigated by exploiting the differences in absorption spectra of light-absorbing materials (Herich et al., 2011; Sandradewi et al., 2008; Zotter et al., 2017). In this method, the aerosol absorption near-ultraviolet and short-visible regions of the spectrum from biomass burning are assumed to be enhanced because of BrC emitted, compared to that from fossil fuel combustion (Kirchstetter et al., 2004; Tian et al., 2019). This makes it possible to derive their contributions to light absorption by using the specific source absorption Ångström exponent (AAE), but the so-called "aethalometer model" could not distinguish as many sources resolved by receptor models due to the similar optical properties of the aerosol sources (Saarikoski et al., 2021). In contrast, receptor models can be utilized to resolve multiple optical source apportionment of aerosol. Several studies used a combination of the receptor model and MLR to indirectly identify sources of aerosol b_{scat}, b_{abs}, and b_{ext} (Cao et al., 2012; Tian et al., 2020; Zhou et al., 2017). For example, Zhou et al. (2017) firstly used positive matrix factorization analysis to quantify the mass contributions of aerosol from secondary aerosol, biomass burning, traffic-related emissions, and coal combustion based on the sole chemical species, and then the MLR was used to apportion the contribution of each source to b_{scat} and b_{abs}. In addition, recent studies have attempted to conduct direct optical source apportionment by combining aerosol chemical species with optical coefficients in one receptor model (Forello et al., 2019; Wang et al., 2020b; Xie et al., 2019). This promising method can provide both chemical and optical profiles in each source to improve the performance of source identification, and may eliminate potential uncertainties caused by the indirect approach.

The Fenwei Plain is designated as the key region of pollution treatment in the "Three-year action plan to fight air pollution" implemented by the Chinese State Council in 2018. As one of the megacities in this plain, Xi'an has been facing severe air pollution problem, especially in winter (Niu et al., 2016; Wang et al., 2015). Here, we conducted high time-resolved aerosol b_{scat} and b_{abs} measurements in Xi'an before and during the city lockdown in China. The main objectives are to (1) characterize the changes of aerosol optical properties since COVID-19 lockdown; (2) quantify the contributions of individual chemical composition and specific source to b_{ext}; and (3) evaluate source-specific aerosol DRE based on a radiative transfer model. This study provides insights into the response of aerosol b_{ext} and DRE to anthropogenic emission sources, which is a scientific basis for establishing future emission control policies to deal with climate change in China.

2 Methodology

2.1 Sampling site and period

Intensive measurements of aerosol optical properties were conducted at one urban sampling site of the National Observation and Research Station of Regional Ecological Environment Change and Comprehensive Management in the

Guanzhong Plain, southwest of Xi'an downtown (34°13' N, 108°52' E, Figure S1). All instruments were placed at the rooftop of an office building (~ 10 m above the ground) and approximately 30 m from the nearest traffic road. A detailed description of the sampling site can be found in Tian et al. (2021). In this study, the sampling campaign consisted of two distinct periods: normal period (January 1st to 23rd, 2020) and COVID-19 lockdown period (January 27th to February 7th, 2020). Three days of January 24th–26th, 2020 were excluded due to the intensive influence of fireworks for the Chinese New Year celebration.

2.2 Measurements

2.2.1 Real-time measurements of b_{scat} and b_{abs}

A single wavelength integrating nephelometer (Aurora 1000, Ecotech, Melbourne, Australia) was carried out to measure aerosol b_{scat} at a wavelength of 525 nm with a 5-min time resolution. In the measurement volume, the ambient air sampled with a flow rate of 5 L min^{-1} was illuminated by the light source, that only light scattered at scattering angles between 10 ° and 170 ° can reach the photomultiplier tube. Thereafter, b_{scat} can be calculated by the proportion of the electrical signals produced by the photomultiplier tube. Span calibration was made using CO_2 to ensure the accuracy of the instrument before sampling, and zero calibration was performed twice each day with particle-free air to subtract the Rayleigh scattering. More detailed principles of the Aurora 1000 have been described elsewhere (Chamberlain-Ward and Sharp, 2011).

Aerosol b_{abs} at wavelengths of 370 nm, 470 nm, 520 nm, 590 nm, 660 nm, and 880 nm were measured by a newly developed Aethalometer (model AE33, Magee Scientific, Berkeley, CA, USA) with a 1-min time resolution. Briefly, the model AE33 was the filter-based absorption photometer that simultaneously measured the light attenuation transmitted through two parallel spots of the aerosol filter with 3.85 L min^{-1} and 1.15 L min^{-1}, respectively. Based on "dual-spot" measurements, it used a real-time loading effect compensation algorithm to eliminate the nonlinear loading effect by increasing the deposition amount of aerosol on the filter. Additionally, a factor of 2.14 was used in the model AE33 to automatically modify the quartz filter matrix scattering effect. A detailed description of this instrument can be found in Drinovec et al. (2015).

Both of the Aurora 1000 and model AE33 instruments equipped with a PM$_{2.5}$ cyclone separator in the sampling inlet to remove particles larger than 2.5 μm, and a Nafion® dryer (MD-700-24S, Perma Pure, Inc., Lakewood, NJ, USA) to retain particles (relative humidity < 40%) before entering these instruments. Considering the relative error (1.5% ±0.1%) between b_{abs} at 520 nm and 525 nm is negligible, the amount of b_{ext} in this study was defined as the sum of b_{scat} at 525 nm and b_{abs} at 520 nm.

2.2.2 Complementary data

A quadrupole aerosol chemical speciation monitor (Q-ACSM, Aerodyne Research Inc., Billerica, Massachusetts, USA) and a Xact 625 ambient metals monitor (Xact 625i, Cooper Environmental Services, Beaverton, OR, USA) were operated to obtain chemical composition characteristics (Furger et al., 2020; Ng et al., 2011). The Q-ACSM measured concentrations of non-refractory species in PM_1 (NO_3^-, SO_4^{2-}, NH_4^+, Cl^-, and OA), and OA was further resolved into POA, less-, and more-oxidized oxygenated OA (LO-OOA and MO-OOA). Detailed information on the Q-ACSM data process and source apportionment of OA can be found in our previous paper (Tian et al., 2021). The Xact 625i quantified hourly element concentrations in $PM_{2.5}$ through X-ray fluorescence analysis, including Si, K, Ca, Cr, Mn, Fe, Zn, As, Se, Ba, Hg, and Pb. Additionally, BC concentration was calculated using b_{abs} at 880 nm (Kirchstetter et al., 2004). Online $PM_{2.5}$ and NO_x concentrations were obtained from the Department of Ecology and Environment of Shaanxi Province. More detailed descriptions of these complementary data can be found in Table S1.

2.3 Meteorological conditions separation

A generalized additive model (GAM) combined with integrated smoothness estimation was used to establish the relationship between b_{ext} and several meteorological parameters as follows (Wood, 2004):

$$\ln b_{ext}(i) = \sum_{j=1}^{7} f_j\big(MP_j(i)\big) + \beta_0 + e_i \tag{1}$$

where $b_{ext}(i)$ is the b_{ext} in Mm^{-1} averaged over the ith hour; MP_j represents the jth meteorological parameter, such as wind speed, wind direction, temperature, pressure, dew point, and planetary boundary layer height, where the data sources can be found in Table S1; f corresponds to the smooth function describing the association between b_{ext} and meteorological parameters; β_0 is the model intercept; and e_i is the regression residuals which is assumed to be normally distributed.

Based on the R package "mgcv" (Wood, 2017), the whole campaign dataset was divided into three parts: a model data (80% of data during the normal period) for establishing the b_{ext} GAM, a test data (20% of data during the normal period) for verifying the accuracy of the model, and a forecast data (100% of data during the lockdown period) for estimating the contributions of meteorological conditions and emissions on b_{ext} reduction.

2.4 Chemical calculation of b_{scat} and b_{abs}

Because of POA and SOA with nonnegligible light scattering and absorbing abilities, the amount of b_{scat} and b_{abs} associated with individual chemical species can be estimated statistically using the ridge regression method:

$$\begin{aligned} b_{scat} = {} & a_1[NH_4NO_3] + a_2[(NH_4)_2SO_4] + a_3[\text{fine soil}] \\ & + a_4[POA] + a_5[LO\text{-}OOA] + a_6[MO\text{-}OOA] + c_1 \end{aligned} \tag{2}$$

$$b_{abs} = b_1[BC] + b_2[POA] + b_3[LO\text{-}OOA] + b_4[MO\text{-}OOA] + c_2 \qquad (3)$$

where b_{scat} and b_{abs} are given in unit of Mm^{-1}; the bracket notation [] represents the specific chemical species concentration in μg m^{-3}; the a_i and b_i ($i = 1$–6) describe the MSE and MAE of each chemical species in the unit of m^2 g^{-1}, respectively; and c_i ($i = 1$ or 2) is the constant. In equation (2), the concentrations of [NH$_4$NO$_3$], [(NH$_4$)$_2$SO$_4$], and [fine soil] were calculated using $1.29 \times$[NO$_3^-$], $1.35 \times$[SO$_4^{2-}$], and [Fe]/0.032, respectively (Chow et al., 2015; CNEMC, 1990). In equation (3), b_1 was calculated by the absorption Ångström exponent method, and the detailed description can be seen in Text S1. The reconstructed [PM] ([PM] = [NH$_4$NO$_3$] + [(NH$_4$)$_2$SO$_4$] + [POA] + [LO-OOA] + [MO-OOA] + [BC] + [fine soil]) is strongly correlated with the measured [PM$_{2.5}$] (R^2 = 0.86), with a slope of 0.79 (Figure S2). That is, the reconstructed [PM] accounted for ~79% of the measured [PM$_{2.5}$]. The NH$_4$NO$_3$, (NH$_4$)$_2$SO$_4$, POA, LO-OOA, and MO-OOA in PM$_{1-2.5}$ are not included in the calculation (equations 2 and 3). A sensitivity analysis concludes that if their concentrations increased by 21% to match the measured PM$_{2.5}$, then the estimated MSEs and MAEs will correspondingly decrease by 21%.

2.5 Hybrid environmental receptor model (HERM) for source apportionment

The source apportionment of b_{ext} was performed with HERM which is a newly developed bilinear model (Chen and Cao, 2018). Briefly, the HERM solves non-negative matrices of unknown factor profiles and contributions with a pre-set number of factors K by iteratively minimizing the object function Q defined as follows:

$$Q = \sum_{j=1}^{J} \sum_{i=1}^{I} \frac{\left(x_{ij} - \sum_{k=1}^{K} g_{ik} f_{kj}\right)^2}{\sigma_{x_{ij}}^2 + \sum_{k=1}^{K} \left(g_{ik}^2 \sigma_{f_{kj}}^2 + \delta_{ik} \sigma_{x_{ij}}^2\right)} \qquad (4)$$

where I, J, and K are the number of samples, aerosol variables, and factors, respectively; the indices of i, j, k represent the sample, aerosol variable, and factor, respectively; x_{ij} is the measured ambient data spectral matrix; f_{kj} is the factor profile matrix; g_{ik} is factor contribution matrix; $\sigma_{x_{ij}}$ and $\sigma_{f_{kj}}$ represent the error in measured ambient data and variability in constrained factor profile, respectively; δ_{ik} is set to 0 or 1 depending on whether the kth factor profile is constrained or unconstrained, respectively.

In this study, both chemical species (PM$_{2.5}$, NO$_3^-$, SO$_4^{2-}$, NH$_4^+$, Cl$^-$, BC, POA, LO-OOA, MO-OOA, Si, K, Ca, Cr, Mn, Fe, Zn, As, Se, Ba, Hg, and Pb in μg m^{-3}) and optical variables (b_{scat} and b_{abs} in Mm^{-1}) were used as input data for the HERM analysis. The uncertainties of hourly ambient data except elements were introduced by the standard deviation of samples with higher time resolution (< 1-hour); the uncertainty of the element was estimated using its concentration, the default analytical relative error (10%) (Rai et al., 2020), and method detection limit (MDL) (Norris et al., 2014) (Text S2). All input variables were classified as strong due to the high signal-to-noise (SNR > 2). Here, the HERM had

predetermined: (1) the ith sample was excluded from source apportionment when missing values occurred in variables; (2) PM$_{2.5}$ value in factor profile was set to unity as a reference standard for both chemical and optical variables.

A range of factor numbers from two to eight was selected to run in the HERM software with completely unconstrained factor profiles, and diagnostic plots are detailed in the supplementary material (Text S3 and Figures S2S3–S7S8). The six-factor solution without mixed source was found to be the optimal solution based on multiple criteria including (1) variations in Q/Q$_{exp}$ that can be used as a metric for choosing the best number of resolved factors (Ulbrich et al., 2009); (2) physical meaningfulness of distinct factor profiles and explained variations (EV) of variables; (3) agreement between the measured and modeled values; and (4) good correlations with external and internal tracers. Detailed information on the final selected factor profiles and contributions are presented in Section 3.4.

2.6 DRE calculations

The Santa Barbara DISORT Atmospheric Radiative Transfer (SBDART) developed by the Institute for Computational Earth System Science, University of California was utilized to estimate the source-specific aerosol DRE. It can calculate the downwelling and upwelling radiative flux (F$_{down}$ and F$_{up}$), in which the difference indicates the net radiative flux (ΔF = F$_{down}$ − F$_{up}$). A detailed description of the SBDART can be found in Ricchiazzi et al. (1998). Based on the optical source apportionment results, the SBDART model input values of aerosol optical depth, SSA, asymmetry factor, and optical coefficients were retrieved using the Optical Properties of Aerosol and Cloud (OPAC) model (Hess et al., 1998). The aerosol DRE can be calculated as follows:

$$DRE_{atmosphere} = DRE_{top} - DRE_{surface} \tag{5}$$

$$DRE_{top} = \Delta F_{top}(\text{with aerosol}) - \Delta F_{top}(\text{without aerosol}) \tag{6}$$

$$DRE_{surface} = \Delta F_{surface}(\text{with aerosol}) - \Delta F_{surface}(\text{without aerosol}) \tag{7}$$

where the indices of atmosphere, top, and surface indicate the DRE in the atmosphere, at the top of the atmosphere, and the earth's surface, respectively; ΔF(with aerosol) and ΔF(without aerosol) represent the net radiative flux with and without aerosol, respectively.

3 Results and discussion

3.1 General descriptions of aerosol optical properties

The temporal variations of hourly mean b_{scat}, b_{abs}, b_{ext}, and SSA together with PM$_{2.5}$ mass concentrations for the entire sampling period are depicted in Figure 1, while a statistics summary of optical and chemical parameters during the

7

normal and COVID-19 lockdown periods is shown in Table 1. The optical coefficients decreased dramatically in accord with the significant reduction of $PM_{2.5}$ since stringent control measures on emission sources were implemented during the lockdown period (Tian et al., 2021; Zheng et al., 2020). The mean values of b_{scat}, b_{abs}, and b_{ext} during the normal period were 688.1 $\pm$261.4 Mm^{-1}, 86.6 $\pm$43.0 Mm^{-1}, and 774.7 $\pm$298.1 Mm^{-1}, respectively, which are consistent with the values (657.4 $\pm$436.9 Mm^{-1}, 104.0 $\pm$69.6 Mm^{-1}, and 761.4 $\pm$506.5 Mm^{-1}) reported previously in winter of 2009 in Xi'an (Cao et al., 2012), even though a series of nationwide air quality standards and long-term pollution control policies have been implemented in the 74 major cities since 2013 (Xu et al., 2020b; Zheng et al., 2018). Comparatively, the kind of control measures aiming to curb the outbreaks did not last long, but it was unprecedentedly strictest in China. The large decreases (27.6–47.0%) were found in b_{scat}, b_{abs}, and b_{ext} in the lockdown (498.4 $\pm$159.0 Mm^{-1}, 45.9 $\pm$22.9 Mm^{-1}, and 544.3 $\pm$ 179.4 Mm^{-1}, respectively), providing insights into the role of anthropogenic emissions on aerosol optical properties.

The SSA defined as the ratio of b_{scat} to b_{ext} increased from 0.89 $\pm$0.03 during the normal period to 0.92 $\pm$0.02 during the lockdown period. As presented in Figure 2a and b, SSA showed linear increases with the mass fractions of secondary inorganic aerosol (SIA = NH_4NO_3 + $(NH_4)_2SO_4$) to $PM_{2.5}$ (R^2 = 0.83–0.84) and SOA (SOA = LO-OOA + MO-OOA) to OA (R^2 = 0.94–0.99), indicating an enhanced role of secondary formation in the lockdown. In addition, the correlations of SSA and the ratio of LO-OOA to MO-OOA were established to reveal a more complex influence of SOA on SSA (Figure 2c), which showed negative relationships (R^2 = 0.69–0.79). It indicated that SSA can be impacted by the degree of oxidation on aerosol, and higher scattering and lower absorption abilities are usually found for more oxidized OA (Han et al., 2015; Lee et al., 2014).

3.2 Effects of emission reduction and meteorological conditions on reduced b_{ext}

Figure 3 shows the time series of the measured and GAM-predicted b_{ext} for the model data, test data, and forecast data. As shown in Tables S2 and S3, the constructed GAM with adjusted R^2 value (0.54) can explain 54% of the variation in b_{ext} after incorporating the nonlinear relationships between optical and meteorological parameters. Independent smoothed meteorological variables of the model were statistically significant by according to p values (< 0.05) from F test. Concurvity indices between each independent smoothed parameter were within 0.5, indicating there was no serious multicollinearity (Schimek, 2009).

Before applying the constructed GAM to predict the b_{ext} during the lockdown period, the cross-validation test was used to evaluate the model. For the test data (20% of data during the normal period), the R^2 value of the linear regression and index of agreement (IOA) (Wu et al., 2018) between the measured and GAM-predicted b_{ext} was 0.83 and 0.92, respectively, suggesting a good performance of the constructed GAM. The difference between the measured and GAM-

predicted b_{ext} in the lockdown can be attributed to emission reduction through the implementation of stringent control measures on emission sources. The emission reduction decreased b_{ext} by 299.2 Mm^{-1} during the lockdown period, higher than the decline of measured b_{ext} (230.4 Mm^{-1}) from normal to lockdown periods. It is indicated that the meteorological conditions enhanced b_{ext} by 68.8 Mm^{-1} during the lockdown period, further reflecting the effective control of anthropogenic emissions.

3.3 Contribution of chemical components to b_{ext}

Table 2 presents the estimated MSE and MAE of an individual chemical component during the normal and lockdown periods. NH$_4$NO$_3$ and (NH$_4$)$_2$SO$_4$ had different MSEs, probably due to their different size distributions (Hu et al., 2017; Zhang et al., 2013b; Zhu et al., 2021). The MSEs of NH$_4$NO$_3$ (3.74 ±0.18 m^2 g^{-1}) and (NH$_4$)$_2$SO$_4$ (7.35 ±0.25 m^2 g^{-1}) during the normal period were higher than those (3.23 ±0.18 m^2 g^{-1} and 4.78 ±0.35 m^2 g^{-1}) during the lockdown period. This may be explained by the higher mass loadings and peak diameters of aerosol without control measures (Cheng et al., 2015; Tao et al., 2015). The MAE of BC decreased from 15.00 m^2 g^{-1} to 13.27 m^2 g^{-1} related to the decline of AAE of BC (Text S1). The MSEs and MAEs of OA factors varied widely, from 3.48 m^2 g^{-1} to 12.89 m^2 g^{-1} and from 0.25 m^2 g^{-1} to 0.59 m^2 g^{-1}, respectively, due to the complex chemical variability of OA constituents (Hallquist et al., 2009; Moise et al., 2015). The MSEs of OA increased with oxidation level from POA to MO-OOA. This could be explained by the increased mass diameter of OA with increasing OA oxidation level (Wang et al., 2021; Xu et al., 2015). The MSE of MO-OOA was larger during the lockdown period than that during the normal period, probably related to the enhanced atmospheric oxidation capacity during the lockdown period (Tian et al., 2021), which is found to result in higher aging state of OA with larger diameter (Hu et al., 2016; Zhu et al., 2021).scattering ability of OA increased with oxidation level (from POA to MO-OOA) (Cappa et al., 2011; Flores et al., 2014); however, Tthe dependence on oxidation level of OA MAEs presented a more complex trend. LO-OOA had higher MAE values than those of POA, indicating more BrC chromophores with stronger light-absorbing capacity formed under less-oxidized condition (Zhang et al., 2020). Additionally, the effect of photo-bleaching in the atmosphere that can weaken the light absorption ability of BrC resulted in the reduction of MO-OOA MAEs (Wang et al., 2021).

The b_{ext} reconstructed by chemical compositions was strongly correlated with the measured optical b_{ext} (R^2 = 0.94), with a slope of 0.78Chemical calculation of b_{ext} was confirmed to be a reasonable estimation of aerosol optical coefficients by using chemical components data (Figures S8 and S9). As shown in Figure 4, OA (POA + LO-OOA + MO-OOA) was the largest contributor to b_{ext} in both periods, accounting for 45.1–61.4%, followed by NH$_4$NO$_3$ (16.5–24.1%), BC (9.3–13.1%), (NH$_4$)$_2$SO$_4$ (7.9–11.2%), and fine soil (4.9–6.5%). This result was different from previous findings that SIA was often the largest contributor to b_{ext} in China, such as Beijing (46–54%) (Han et al., 2015), Chengdu (43%) (Tao et al., 2014), Nanjing (53%) (Shen et al., 2014), and Xi'an (63%) (Cao et al., 2012), highlighting the dominant role of organic

265 matters in aerosol light extinction in Xi'an today. Compared to the normal period, the contributions of NH_4NO_3, $(NH_4)_2SO_4$, fine soil, and BC, and POA to b_{ext} decreased by 1.3–7.6% in the lockdown, whereas contributions of two SOAs to b_{ext} increased by 3.0–14.6%. On the one hand, the mass concentrations of LO-OOA and MO-OOA decreased by 20.9–34.7% from normal to lockdown periods, lower than those of other chemical species (35.8–72.5%); On the other hand, both of SOAs MSEs and MAEs showed higher values during the lockdown period, especially MO-OOA. The

270 combination of effects eventually led to an enhanced role of SOA in light extinction during the lockdown.

3.4 Contribution of sources to b_{ext}

The six-factor solution was selected to be the optimal solution, which can adequately account for the variability in $PM_{2.5}$ concentration and optical coefficients (Figures S10 and S11). Six sources were determined by the HERM analysis, consisting of traffic-related emission, biomass burning, coal combustion, fugitive dust, nitrate plus SOA source, and

275 sulfate plus SOA source. Details about their characteristics are presented in Figure 5. The first source identified as traffic-related emission was characterized by high EV values of Cr (77%), Mn (53%), Fe (36%), and Zn (39%), which can be released from lubricating oils, fuel additives, and brake and tire wear (Ålander et al., 2005; Geivanidis et al., 2003; Tao et al., 2017; Zhang et al., 2013a). Moderate contributions of POA (26%) and BC (28%) were commonly regarded as species of diesel and gasoline engine exhaust (Chow et al., 2004; Liu et al., 2017). Additionally, the temporal variations

280 in b_{ext} from this source correlated well with NO_x ($R^2 = 0.72$), suggesting an association with motor vehicle emissions (Huang et al., 2017; Li et al., 2017a). The second source with high EV values of POA (45%), LO-OOA (41%), BC (32%), Cl (34%), and K (41%) was judged to be biomass burning. K was regarded as an excellent tracer of biomass burning (Li et al., 2007; Ni et al., 2017), and good correlations were also found between b_{ext} from biomass burning and K ($R^2 = 0.64$). Previous studies have shown that POA from biomass burning can be rapidly oxidized in the atmosphere

285 (Cubison et al., 2011), therefore, the abundant LO-OOA observed in this source might be indicative of aged biomass-burning aerosol (Crippa et al., 2013; Kim et al., 2017; Xu et al., 2015). The third source, coal combustion, was characterized by high EV values of Cl (42%), As (38%), Se (46%), and Pb (25%). Of these elements, As and Se were enriched in coals (Tian et al., 2013), which were reliable indicators for coal combustion (Tan et al., 2017; Yu et al., 2019); and Pb was found to possibly emitted from coal combustion in Xi'an (Xu et al., 2012). The fourth source was

290 defined as fugitive dust due to significant EV values of Si (92%), Ca (63%), and Fe (31%), which were the dominant chemical species in natural and construction dust profiles (Liu et al., 2017; Zhao et al., 2006). Two secondary sources were resolved in our study as nitrate plus SOA source with high EV values of NO_3^- (42%), NH_4^+ (33%), and MO-OOA (34%) and sulfate plus SOA source with high EV values of SO_4^{2-} (58%) and MO-OOA (39%), respectively. Since SO_2 oxidation to sulfate needs a long time (e.g., 1 week) at the typical atmospheric level of OH radicals, SO_4^{2-} was likely

295 associated with the regional source, while NO_3^- was often formed more locally due to the intense NO_x emissions in China

(Zhang et al., 2015; Zheng et al., 2014). The defined nitrate and sulfate plus SOA sources appeared to have stronger associations with local and regional processes, respectively.

As shown in Figure 6, the average b_{ext} from traffic-related emission, coal combustion and fugitive dust decreased from 77.3 $\pm$46.8 Mm^{-1}, 73.6 $\pm$60.9 Mm^{-1}, and 93.3 $\pm$82.7 Mm^{-1} during the normal period to 1.7 $\pm$4.0 Mm^{-1}, 38.5 $\pm$34.5 Mm^{-1}, and 30.8 $\pm$24.4 Mm^{-1} during the lockdown period, respectively, which can be explained by traffic restriction, closure of industries and stopping construction activities. b_{ext} from traffic-related emission with the largest reduction (97.9%) emphasized the effectiveness of controlling private gasoline cars and commercial and construction diesel trucks in the lockdown (Wang et al., 2020c). For two secondary sources, though previous studies reported the enhancement of secondary aerosol formation efficiencies as the increase of atmospheric oxidation capacity in the lockdown (Huang et al., 2020; Le et al., 2020; Tian et al., 2021), the decreases in gas and organic precursors (e.g., NO_2, SO_2, and VOCs) led to the 47.5% and 21.4% reductions of b_{ext} from sources of nitrate plus SOA and sulfate plus SOA, respectively. That is, the enhanced secondary aerosol cannot offset the primary emission reduction in Xi'an, confirming that reducing anthropogenic primary emissions is still the most effective treatment of aerosol pollution.

By contrast, the average b_{ext} from biomass burning during the lockdown period (215.4 $\pm$ 163.9 Mm^{-1}) was higher than that during the normal period (169.4 $\pm$ 196.9 Mm^{-1}). The government didn't strengthen the past control policies that forbade biomass burning in the lockdown. Moreover, strict controls were enforced on the movements of people, even in the countryside, possibly resulting more consumption of biomass for cooking and heating. As shown in Figure 7, the rising stages of PM$_{2.5}$ during the lockdown period were all accompanied by the increase in b_{ext} from biomass burning, accounting for 46.4–55.6% of the total b_{ext}. Take the rising stage of PM$_{2.5}$ from 13:00 30 to 7:00 31 January as an example, b_{ext} from POA and LO-OOA increased rapidly at rates of 8.6 Mm^{-1} hour^{-1} and 8.2 Mm^{-1} hour^{-1}, respectively. Correspondingly, b_{ext} from biomass burning showed the fastest rise (26.0 Mm^{-1} hour^{-1}) in all primary sources, which led to biomass burning becoming the most important source to b_{ext} (36.7%) in the lockdown (Figure 6). Hence, additional actions and investigations on biomass burning emissions would be taken into consideration.

3.5 Impacts of COVID-19 lockdown on aerosol DRE

Figure 8 shows the range of source-specific aerosol DRE$_{top}$, DRE$_{surface}$, and DRE$_{atmosphere}$ during the normal and lockdown periods. For all sources, the aerosol DRE$_{atmosphere}$ values in both periods were positive, producing net warming effects in the atmosphere. The mean aerosol DRE$_{atmosphere}$ decreased from 31.0 $\pm$23.2 W m^{-2} before the lockdown to 14.1 $\pm$11.5 W m^{-2} in the lockdown, with a reduction of 54.5%. This can be explained by the reduced aerosol concentration and increased SSA (Liu et al., 2020).

325   With regard to the contributions of specific sources on the $DRE_{atmosphere}$, traffic-related emission had the largest positive effect on $DRE_{atmosphere}$ during the normal period, with the value of 13.3 ±9.2 W m^{-2}, followed by biomass burning (8.4 ±13.0 W m^{-2}), coal combustion (7.8 ±7.2 W m^{-2}), sulfate plus SOA source (1.7 ±3.0 W m^{-2}), and fugitive dust (1.1 ± 2.4 W m^{-2}). Nitrate and plus SOA source presented the negative value of $DRE_{atmosphere}$ (-1.2 ±0.7 W m^{-2}), suggesting the cooling effect in the atmosphere. Due to the strictest traffic restrictions implemented, the $DRE_{atmosphere}$ from traffic-
330   related emission (0.4 ±1.0 W m^{-2}) showed a significant reduction (97.0%) in the lockdown. However, the $DRE_{atmosphere}$ from biomass burning increased to 10.0 ±10.9 W m^{-2}, indicating that biomass burning was not effectively controlled during the lockdown period. The other four sources contributed relatively small amounts of $DRE_{atmosphere}$; that is 4.5 ± 4.5 W m^{-2} for coal combustion, -0.3 ±0.8 W m^{-2} for fugitive dust, -1.4 ±0.8 W m^{-2} for nitrate plus SOA source, and 1.0 ±1.8 W m^{-2} for sulfate plus SOA source. Similar to Xi'an city, the pollution sources of traffic and biomass burning were
335   the two most significant anthropogenic sources of aerosol in most Chinese cities, such as Chengdu, Guangzhou, Jinan, Tianjin, and etc (Cheng et al., 2021; Huang et al., 2018; Khan et al., 2021; Li et al., 2017b). The results in this study indicated that the control measures on traffic in the lockdown were highly effective for mitigating the effects of climate change in the short term, while future emission control policies should consider the importance of biomass burning to tackle climate change in China.

340   **4 Conclusion**

This study conducted an intensive real-time measurement campaign in an urban city of China before and during the lockdown of Coronavirus Disease 2019 to investigate the impacts of anthropogenic emissions on aerosol optical properties and direct radiative effect (DRE). Decreases in light scattering coefficient (b_{scat}), light absorption coefficient (b_{abs}), and light extinction coefficient (b_{ext}) were observed in the lockdown with reductions of 27.6–47.0%, in accord
345   with the decline of $PM_{2.5}$ under strict emission control measures. Single scattering albedo during the lockdown period (0.92 ±0.02) was higher than that during the normal period (0.89 ±0.03), suggesting an enhanced role of secondary formation in the lockdown. The generalized additive model analysis showed that meteorological conditions enhanced b_{ext} by 68.8 Mm^{-1} during the lockdown period, thus, the dramatical reduction of b_{ext} was credited to anthropogenic emission reductions.

350   The relationship between b_{ext} and chemical components was established based on the ridge regression analysis. Using the estimated mass scattering and absorption efficiencies (MSEs and MAEs) of chemical components, OA including primary OA, less-, and more-oxidized oxygenated OA was found to be the largest contributor (45.1–61.4%) to b_{ext} before and during the lockdown period, followed by NH_4NO_3 (16.5–24.1%), BC (9.3–13.1%), $(NH_4)_2SO_4$ (7.9–11.2%), and

fine soil (4.9–6.5%). Particularly, secondary OA played an increasingly important part in light extinction during the lockdown when contributions of two oxygenated OAs to b_{ext} increased by 3.0–14.6%.

A hybrid environmental receptor model coupled with chemical and optical variables was utilized to carry out optical source apportionment. Six sources of b_{ext} were resolved, including traffic-related emission, biomass burning, coal combustion, fugitive dust, nitrate plus SOA source, and sulfate plus SOA source. Most sources showed reductions of b_{ext} (21.4–97.9%) during the lockdown, confirming the effectiveness of reducing anthropogenic primary emissions for treating aerosol pollution. b_{ext} from traffic-related emission had the most evident decrement (97.9%), whereas that from biomass burning increased by 27.1% during the lockdown due to the undiminished needs of residential cooking and heating in winter.

The atmospheric radiative transfer further illustrated that aerosol produced net warming effects (14.1–31.0 W m^{-2}) in the atmosphere during the normal and lockdown periods. Biomass burning instead of traffic-related emission became the largest positive effect (10.0 ± 10.9 W m^{-2}) on aerosol DRE in the atmosphere in the lockdown. The results implied that reducing biomass burning would be another direct and effective way of climate change mitigation besides traffic restriction, therefore, the Chinese government should further tighten the policy on controlling biomass burning in the future.

Competing interests. The authors declare that they have no conflict of interest.

Author contributions. QW, YH, and JC designed the campaign. SL, YZ, and WR conducted field measurements. JT, HL, and YM made data analysis and interpretation. JT wrote the paper with contributions from all co-authors.

References

Ålander, T., Antikainen, E., Raunemaa, T., Elonen, E., Rautiola, A., and Torkkell, K.: Particle emissions from a small two-stroke engine: Effects of fuel, lubricating oil, and exhaust aftertreatment on particle characteristics, Aerosol Sci. Tech., 39, 151–161, https://doi.org/1 0.1080/027868290910224, 2005.

Andreae, M. O. and Gelencsér, A.: Black carbon or brown carbon? The nature of light-absorbing carbonaceous aerosols, Atmos. Chem. Phys., 6, 3131–3148, https://doi.org/10.5194/acp-6-3131-2006, 2006.

Bellouin, N., Quaas, J., Morcrette, J. J., and Boucher, O.: Estimates of aerosol radiative forcing from the MACC re-analysis, Atmos. Chem. Phys., 13, 2045–2062, https://doi.org/10.5194/acp-13-2045-2013, 2013.

390 Cao, J. J., Wang, Q. Y., Chow, J. C., Watson, J. G., Tie, X. X., Shen, Z. X., Wang, P., and An, Z. S.: Impacts of aerosol compositions on visibility impairment in Xi'an, China, Atmos. Environ., 59, 559–566, https://doi.org/10.1016/j.atmosenv.2012.05.036, 2012.

~~Cappa, C. D., Che, D. L., Kessler, S. H., Kroll, J. H., and Wilson, K. R.: Variations in organic aerosol optical and hygroscopic properties upon heterogeneous OH oxidation, J. Geophys. Res. Atmos., 116, D15204,~~
395 ~~https://doi.org/10.1029/2011JD015918, 2011.~~

Chamberlain-Ward, S. and Sharp, F.: Advances in Nephelometry through the Ecotech Aurora Nephelometer, The Scientific World Journal, 11, 2530–2535, https://doi.org/10.1100/2011/310769, 2011.

Chen, L. W. and Cao, J.: $PM_{2.5}$ source apportionment using a Hybrid Environmental Receptor Model, Environ. Sci. Technol., 52, 6357–6369, https://doi.org/10.1021/acs.est.8b00131, 2018.

400 Chen, Y., Zhang, S. M., Peng, C., Shi, G. M., Tian, M., Huang, R. J., Guo, D. M., Wang, H. B., Yao, X. J., and Yang, F. M.: Impact of the COVID-19 pandemic and control measures on air quality and aerosol light absorption in southwestern China, Sci. Total Environ., 749, 141419, https://doi.org/10.1016/j.scitotenv.2020.141419, 2020.

Cheng, M. T., Tang, G. Q., Lv, B., Li, X. R., Wu, X. R., Wang, Y. M., and Wang, Y. S.: Source apportionment of $PM_{2.5}$ and visibility in Jinan, China, J. Environ. Sci., 102, 207–215, https://doi.org/10.1016/j.jes.2020.09.012, 2021.

405 Cheng, Z., Jiang, J. K., Chen, C. H., Gao, J., Wang, S. X., Watson, J. G., Wang, H. L., Deng, J. G., Wang, B. Y., Zhou, M., Chow, J. C., Pitchford, M. L., and Hao, J. M.: Estimation of aerosol mass scattering efficiencies under high mass loading: Case study for the megacity of Shanghai, China, Environ. Sci. Technol., 49, 831–838, https://doi.org/10.1021/es504567q, 2015.

China National Environmental Monitoring Centre (CNEMC).: Background values of soil elements in China, Chinese
410 Environmental Press, Beijing (in Chinese), 1990.

Chow, J. C., Lowenthal, D. H., Chen, L. W. A., Wang, X. L., and Watson, J. G.: Mass reconstruction methods for $PM_{2.5}$: a review, Air Qual. Atmos. Health, 8, 243–263, https://doi.org/10.1007/s11869-015-0338-3, 2015.

Chow, J. C., Watson, J. G., Kuhns, H., Etyemezian, V., Lowenthal, D. H., Crow, D., Kohl, S. D., Engelbrecht, J. P., and Green, M. C.: Source profiles for industrial, mobile, and area sources in the Big Bend Regional Aerosol Visibility
415 and Observational study, Chemosphere, 54, 185–208, https://doi.org/10.1016/j.chemosphere.2003.07.004, 2004.

Crippa, M., DeCarlo, P. F., Slowik, J. G., Mohr, C., Heringa, M. F., Chirico, R., Poulain, L., Freutel, F., Sciare, J., Cozic, J., Di Marco, C. F., Elsasser, M., Nicolas, J. B., Marchand, N., Abidi, E., Wiedensohler, A., Drewnick, F., Schneider, J., Borrmann, S., Nemitz, E., Zimmermann, R., Jaffrezo, J. L., Prévôt, A. S. H., and Baltensperger, U.: Wintertime aerosol chemical composition and source apportionment of the organic fraction in the metropolitan area of Paris,
420 Atmos. Chem. Phys., 13, 961–981, https://doi.org/10.5194/acp-13-961-2013, 2013.

Cubison, M. J., Ortega, A. M., Hayes, P. L., Farmer, D. K., Day, D., Lechner, M. J., Brune, W. H., Apel, E., Diskin, G. S., Fisher, J. A., Hecobian, A., Knapp, D. J., Mikoviny, T., Riemer, D., Sachse, G. W., Sessions, W., Weber, R. J., Weinheimer, A. J., and Jimenez, J. L.: Effects of aging on organic aerosol from open biomass burning smoke in aircraft and lab studies, Atmos. Chem. Phys., 11, 12049–12064, https://doi.org/10.5194/acpd-11-12103-2011, 2011.

425 Deng, J. J., Zhang, Y. R., Hong, Y. W., Xu, L. L., Chen, Y. T., Du, W. J., and Chen, J. S.: Optical properties of PM2.5 and the impacts of chemical compositions in the coastal city Xiamen in China, Sci. Total Environ., 557–558, 665–675, https://doi.org/10.1016/j.scitotenv.2016.03.143, 2016.

Drinovec, L., Močnik, G., Zotter, P., Prévôt, A. S. H., Ruckstuhl, C., Coz, E., Rupakheti, M., Sciare, J., Müller, T., Wiedensohler, A., and Hansen, A. D. A.: The "dual-spot" Aethalometer: an improved measurement of aerosol black
430   carbon with real-time loading compensation, Atmos. Meas. Tech., 8, 1965–1979, https://doi.org/10.5194/amt-8-1965-2015, 2015.

Feng, Y., Ramanathan, V., and Kotamarthi, V. R.: Brown carbon: a significant atmospheric absorber of solar radiation? Atmos. Chem. Phys., 13, 8607–8621, https://doi.org/10.5194/acp-13-8607-2013, 2013.

~~Flores, J. M., Zhao, D. F., Segev, L., Schlag, P., Kiendler-Scharr, A., Fuchs, H., Watne, A. K., Bluvshtein, N., Mentel,~~
435   ~~T. F., and Hallquist, M.: Evolution of the complex refractive index in the UV spectral region in ageing secondary~~
        ~~organic aerosol, Atmos. Chem. Phys., 14, 5793–5806, https://doi.org/10.5194/acp-14-5793-2014, 2014.~~

Forello, A. C., Bernardoni, V., Calzolai, G., Lucarelli, F., Massabò, D., Nava, S., Pileci, R. E., Prati, P., Valentini, S., Valli, G., and Vecchi, R.: Exploiting multi-wavelength aerosol absorption coefficients in a multi-time resolution source apportionment study to retrieve source-dependent absorption parameters, Atmos. Chem. Phys., 19, 11235–
440   11252, https://doi.org/10.5194/acp-19-11235-2019, 2019.

Furger, M., Rai, P., Slowik, J. G., Cao, J. J., Visser, S., Baltensperger, U., and Prévôt, A. S. H.: Automated alternating sampling of PM10 and PM2.5 with an online XRF spectrometer, Atmos. Environ.: X, 5, 100065, https://doi.org/10.1016/j.aeaoa.2020.100065, 2020.

Geivanidis, S., Pistikopoulos, P., and Samaras, Z.: Effect on exhaust emissions by the use of methylcyclopentadienyl
445   manganese tricarbonyl (MMT) fuel additive and other lead replacement gasolines, Sci. Total Environ., 305, 129–141, https://doi.org/10.1016/S0048-9697(02)00476-X, 2003.

Hallquist, M., Wenger, J. C., Baltensperger, U., Rudich, Y., Simpson, D., Claeys, M., Dommen, J., Donahue, N. M., George, C., Goldstein, A. H., Hamilton, J. F., Herrmann, H., Hoffmann, T., Iinuma, Y., Jang, M., Jenkin, M. E., Jimenez, J. L., Kiendler-Scharr, A., Maenhaut, W., McFiggans, G., Mentel, Th. F., Monod, A., Prévôt, A. S. H.,
450   Seinfeld, J. H., Surratt, J. D., Szmigielski, R., and Wildt, J.: The formation, properties and impact of secondary organic aerosol: current and emerging issues, Atmos. Chem. Phys., 9, 5155–5236, https://doi.org/10.5194/acp-9-5155-2009, 2009.

Han, T. T., Xu, W. Q., Chen, C., Liu, X. G., Wang, Q. Q., Li, J., Zhao, X. J., Du, W., Wang, Z. F., and Sun, Y. L.: Chemical apportionment of aerosol optical properties during the Asia-Pacific Economic Cooperation summit in
455   Beijing, China, J. Geophys. Res.-Atmos., 120, 12281–12295, https://doi.org/10.1002/2015JD023918, 2015.

Herich, H., Hueglin, C., and Buchmann, B.: A 2.5 year's source apportionment study of black carbon from wood burning and fossil fuel combustion at urban and rural sites in Switzerland, Atmos. Meas. Tech., 4, 1409–1420, https://doi.org/10.5194/amt-4-1409-2011, 2011.

Hess, M., Koepke, P., and Schult, I.: Optical properties of aerosols and clouds: The software package OPAC, B. Am.
460   Meteorol. Soc., 79, 831–844, https://doi.org/10.1175/1520-0477(1998)079<0831:OPOAAC>2.0.CO;2, 1998.

Hu, W., Hu, M., Hu, W. W., Zheng, J., Chen, C., Wu, Y. S., and Guo, S.: Seasonal variations in high time-resolved chemical compositions, sources, and evolution of atmospheric submicron aerosols in the megacity Beijing, Atmos. Chem. Phys., 17, 9979–10000, https://doi.org/10.5194/acp-17-9979-2017, 2017.

Hu, W. W., Hu, M., Hu, W., Jimenez, J. L., Yuan, B., Chen, W. T., Wang, M., Wu, Y. S., Chen, C., Wang, Z. B., Peng,
465   J. F., Zeng, L. M., and Shao, M.: Chemical composition, sources, and aging process of submicron aerosols in Beijing:

Contrast between summer and winter, J. Geophys. Res.-Atmos., 121, 1955–1977, https://doi.org/10.1002/2015JD024020, 2016.

Huang, X., Ding, A. J., Gao, J., Zheng, B., Zhou, D. R., Qi, X. M., Tang, R., Wang, J. P., Ren, C. H., Nie, W., Chi, X. G., Xu, Z., Chen, L. D., Li, Y. Y., Che, F., Pang, N. N., Wang, H. K., Tong, D., Qin, W., Cheng, W., Liu, W. J., Fu, Q. Y., Liu, B. X., Chai, F., Davis, J. S., Zhang, Q., and He, K. B.: Enhanced secondary pollution offset reduction of primary emissions during COVID-19 lockdown in China, Natl. Sci. Rev., 8, nwaa137, https://doi.org/10.1093/nsr/nwaa137, 2020.

Huang, X. F., Zou, B. B., He, L. Y., Hu, M., Prévôt, A. S. H., and Zhang, Y. H.: Exploration of $PM_{2.5}$ sources on the regional scale in the Pearl River Delta based on ME-2 modeling, Atmos. Chem. Phys., 18, 11563–11580, https://doi.org/10.5194/acp-18-11563-2018, 2018.

Huang, X. J., Liu, Z. R., Liu, J. Y., Hu, B., Wen, T. X., Tang, G. Q., Zhang, J. K., Wu, F. K., Ji, D. S., Wang, L. L., and Wang, Y. S.: Chemical characterization and source identification of $PM_{2.5}$ at multiple sites in the Beijing-Tianjin-Hebei region, China, Atmos. Chem. Phys., 17, 12941–12962, https://doi.org/10.5194/acp-17-12941-2017, 2017.

Ibrahim, S., Landa, M., Pešek, O., Pavelka, K., and Halounova, L.: Space-time machine learning models to analyze COVID-19 pandemic lockdown effects on aerosol optical depth over Europe, Remote Sens., 13, 3027, https://doi.org/10.3390/rs13153027, 2021.

IPCC: Climate change 2013: The physical science basis. Contribution of working group I to the fifth assessment reprot of the intergovemental panel on climate change [Stocker, T. F., D. Qin, G. -K. Plattner, M. Tignor, S. K. Allen, J. Boschung, A. Nauels, Y. Xia, V. Bex and P.M. Midgley (eds.)]. Cambridage University Press, Cambrigde, United Kingdom and New York, NY, USA, 1535pp, 2013.

Khan, J. Z., Sun, L., Tian, Y. Z., Shi, G. L., and Feng, Y. C.: Chemical characterization and source apportionment of PM_1 and $PM_{2.5}$ in Tianjin, China: Impacts of biomass burning and primary biogenic sources, J. Environ. Sci., 99, 196–209, https://doi.org/10.1016/j.jes.2020.06.027, 2021.

Kim, H., Zhang, Q., Bae, G. N., Kim, J. Y., and Lee, S. B.: Sources and atmospheric processing of winter aerosols in Seoul, Korea: Insights from real-Time measurements using a high-resolution aerosol mass spectrometer, Atmos. Chem. Phys., 17, 2009–2033, https://doi.org/10.5194/acp-17-2009-2017, 2017.

Kirchstetter, T.W., Novakov, T., and Hobbs, P. V.: Evidence that the spectral dependence of light absorption by aerosols is affected by organic carbon, J. Geophys. Res.-Atmos., 109, D21208, doi:10.1029/2004JD004999, 2004.

Kumar, D., Singh, A. K., Kumar, V., Poyoja, R., Ghosh, A., and Singh, B.: COVID-19 driven changes in the air quality; a study of major cities in the Indian state of Uttar Pradesh, Environ. Pollut., 274, 116512, https://doi.org/10.1016/j.envpol.2021.116512, 2021.

Laskin, A., Laskin, J., and Nizkorodov, S. A.: Chemistry of atmospheric brown carbon, Chem. Rev., 115, 10, 4335–4382, https://doi.org/10.1021/cr5006167, 2015.

Le, T. H., Wang, Y., Liu, L., Yang, J. N., Yung, Y., Li, G. H., and Seinfeld, J. H.: Unexpected air pollution with marked emission reductions during the COVID-19 outbreak in China, Science, 369, 702–706, https://doi.org/10.1126/science.abb7431, 2020.

Lee, H. J., Aiona, P. K., Laskin, A., Laskin, J., and Nizkorodov, S. A.: Effect of solar radiation on the optical properties and molecular composition of laboratory proxies of atmospheric brown carbon, Environ. Sci. Technol., 48, 10217–10226, https://doi.org/10.1021/es502515r, 2014.

Li, H. Y., Zhang, Q., Zhang, Q., Chen, C. R., Wang, L. T., Wei, Z., Zhou, S., Parworth, C., Zheng, B., Canonaco, F., Prévôt, A. S. H., Chen, P., Zhang, H. L., Wallington, T. J., and He, K. B.: Wintertime aerosol chemistry and haze

evolution in an extremely polluted city of the North China Plain: significant contribution from coal and biomass combustion, Atmos. Chem. Phys., 17, 4751–4768, https://doi.org/10.5194/acp-17-4751-2017, 2017a.

Li, L., Li, Q., Huang, L., Wang, Q., Zhu, A. S., Xu, J., Liu, Z. Y., Li, H. L., Shi, L. S., Li, R., Azari, M., Wang, Y. J., Zhang, X. J., Liu, Z. Q., Zhu, Y. H., Zhang, K., Xue, S. H., Ooi, M. C. G., Zhang, D. P., and Chan, A.: Air quality changes during the COVID-19 lockdown over the Yangtze River Delta Region: An insight into the impact of human activity pattern changes on air pollution variation, Sci. Total Environ., 732, 139282, https://doi.org/10.1016/j.scitotenv.2020.139282, 2020.

Li, L. L, Tan, Q. W., Zhang, Y. H., Feng, M., Qu, Y., An, J. L., and Liu, X. G.: Characteristics and source apportionment of PM$_{2.5}$ during persistent extreme haze events in Chengdu, southwest China, Environ. Pollut., 230, 718–729, https://doi.org/10.1016/j.envpol.2017.07.029, 2017b.

Li, X. H., Wang, S. X., Duan, L., Hao, J. M., Li, C., Chen, Y. S., and Yang, L.: Particulate and trace gas emissions from open burning of wheat straw and corn stover in China, Environ. Sci. Technol., 41, 6052–6058, https://doi.org/10.1021/es0705137, 2007.

Lin, G. X., Penner, J. E., Flanner, M. G., Sillman, S., Xu, L., and Zhou, C.: Radiative forcing of organic aerosol in the atmosphere and on snow: Effects of SOA and brown carbon, J. Geophys. Res.-Atmos., 119, 7453–7476, https://doi.org/10.1002/2013JD021186, 2014.

Lin, Y. C., Zhang, Y. L., Xie, F., Fan, M. Y., and Liu, X.: Substantial decreases of light absorption, concentrations and relative contributions of fossil fuel to light-absorbing carbonaceous aerosols attributed to the COVID-19 lockdown in east China, Environ. Pollut., 275, 116615, https://doi.org/10.1016/j.envpol.2021.116615, 2021.

Liu, B. S., Wu, J. H., Zhang, J. Y., Wang, L., Yang, J. M., Liang, D. N., Dai, Q. L., Bi, X. H., Feng, Y. C., Zhang, Y. F., and Zhang, Q. X.: Characterization and source apportionment of PM$_{2.5}$ based on error estimation from EPA PMF 5.0 model at a medium city in China, Environ. Pollut., 222, 10–22, https://doi.org/10.1016/j.envpol.2017.01.005, 2017.

Liu, D. T., Hu, K., Zhao, D. L., Ding, S., Wu, Y. F., Zhou, C., Yu, C. J., Tian, P., Liu, Q., Bi, K., Wu, Y. Z., Hu, B., Ji, D. S., Kong, S. F., Ouyang, B., He, H., Huang, M. Y., and Ding, D. P.: Efficient vertical transport of black carbon in the planetary boundary layer, Geophys. Res. Lett., 47, e2020GL088858, https://doi.org/10.1029/2020GL088858, 2020.

Ma, X., Yu, F., and Luo, G.: Aerosol direct radiative forcing based on GEOS-Chem-APM and uncertainties, Atmos. Chem. Phys., 12, 5563–5581, https://doi.org/10.5194/acp-12-5563-2012, 2012.

Malm, W. C. and Hand, J. L.: An examination of the physical and optical properties of aerosols collected in the IMPROVE program, Atmos. Environ., 41, 3407–3427, https://doi.org/10.1016/j.atmosenv.2006.12.012, 2007.

Moise, T., Flores, J. M., and Rudich, Y.: Optical properties of secondary organic aerosols and their changes by chemical processes, Chem. Rev., 115, 4400–4439, https://doi.org/10.1021/cr5005259, 2015.

Ng, N. L., Herndon, S. C., Trimborn, A., Canagaratna, M. R., Croteau, P. L., Onasch, T. B., Sueper, D., Worsnop, D. R., Zhang, Q., Sun, Y. L., and Jayne, J. T.: An aerosol chemical speciation monitor (ACSM) for routine monitoring of the composition and mass concentrations of ambient aerosol, Aerosol Sci. Technol., 45, 780–794, https://doi.org/10.1080/02786826.2011.560211, 2011.

Ni, H. Y., Tian, J., Wang, X. L., Wang, Q. Y., Han, Y. M., Cao, J. J., Long, X., Chen, L.-W. A., Chow, J. C., and Watson, J. G.: PM$_{2.5}$ emissions and source profiles from open burning of crop residues, Atmos. Environ., 169, 229–237, https://doi.org/10.1016/j.atmosenv.2017.08.063, 2017.

Niu, X. Y., Cao, J. J., Shen, Z. X., Ho, S. S. H., Tie, X. X., Zhao, S. Y., Xu, H. M., Zhang, T., and Huang, R. J.: $PM_{2.5}$ from the Guanzhong Plain: Chemical composition and implications for emission reductions, Atmos. Environ., 147, 458–469, https://doi.org/10.1016/j.atmosenv.2016.10.029, 2016.

550 Norris, G., Duvall, R., Brown, S., and Bai, S.: EPA positive matrix factorization (PMF) 5.0 fundamentals and user guide, 2014.

Qin, Y. M., Tan, H. B., Li, Y. J., Li, Z. J., Schurman, M. I., Liu, L., Wu, C., and Chan, C. K.: Chemical characteristics of brown carbon in atmospheric particles at a suburban site near Guangzhou, China, Atmos. Chem. Phys., 18, 16409–16418, https://doi.org/10.5194/acp-18-16409-2018, 2018.

555 Rai, P., Furger, M., Slowik, J. G., Canonaco, F., Fröhlich, R., Hüglin, C., Minguillón, M. C., Petterson, K., Baltensperger, U., and Prévôt, A. S. H.: Source apportionment of highly time-resolved elements during a firework episode from a rural freeway site in Switzerland, Atmos. Chem. Phys., 20, 1657–1674, https://doi.org/10.5194/acp-20-1657-2020, 2020.

Ricchiazzi, P., Yang, S. R., Gautier, C., and Sowle, D.: SBDART: A research and teaching software tool for Plane-560 parallel radiative transfer in the Earth's atmosphere, B. Am. Meteorol. Soc., 79, 2101–2114, https://doi.org/10.1175/1520-0477(1998)079<2101:SARATS>2.0.CO;2, 1998.

Saarikoski, S., Niemi, J. V., Aurela, M., Pirjola, L., Kousa, A., Rönkkö, T., and Timonen, H.: Sources of black carbon at residential and traffic environments obtained by two source apportionment methods, Atmos. Chem. Phys., 21, 14851–14869, https://doi.org/10.5194/acp-21-14851-2021, 2021.

565 Sanap, S. D.: Global and regional variations in aerosol loading during COVID-19 imposed lockdown, Atmos. Environ., 246, 118132, https://doi.org/10.1016/j.atmosenv.2020.118132, 2021.

Sandradewi, J., Prévôt, A. S. H., Szidat, S., Perron, N., Alfarra, M. R., Lanz, V. A., Weingartner, E., and Baltensperger, U.: Using aerosol light absorption measurements for the quantitative determination of wood burning and traffic emission contributions to particulate matter, Environ. Sci. Technol., 42, 3316–3323, 570 https://doi.org/10.1021/es702253m, 2008.

Schimek, M. G.: Semiparametric penalized generalized additive models for environmental research and epidemiology, Environmetrics, 20, 699–717, https://doi.org/10.1002/env.972, 2009.

Shen, G. F., Xue, M., Yuan, S. Y., Zhang, J., Zhao, Q. Y., Li, B., Wu, H. S., and Ding, A. J.: Chemical compositions and reconstructed light extinction coefficients of particulate matter in a mega-city in the western Yangtze River 575 Delta, China, Atmos. Environ., 83, 14–20, https://doi.org/10.1016/j.atmosenv.2013.10.055, 2014.

Tan, J. H., Zhang, L. M., Zhou, X. M., Duan, J. C., Li, Y., Hu, J. N., and He, K. B.: Chemical characteristics and source apportionment of $PM_{2.5}$ in Lanzhou, China, Sci. Total Environ., 601–602, 1743–1752, https://doi.org/10.1016/j.scitotenv.2017.06.050, 2017.

Tao, J., Zhang, L. M., Cao, J. J., Zhong, L. J., Chen, D. S., Yang, Y. H., Chen, D. H., Chen, L. G., Zhang, Z. S., Wu, Y., 580 Xia, Y. J., Ye, S. Q., and Zhang, R. J.: Source apportionment of $PM_{2.5}$ at urban and suburban areas of the Pearl River Delta region, south China - With emphasis on ship emissions, Sci. Total Environ., 574, 1559–1570, https://doi.org/10.1016/j.scitotenv.2016.08.175, 2017.

Tao, J., Zhang, L. M., Cao, J., Hsu, S. C., Xia, X. G., Zhang, Z. S., Lin, Z. J., Cheng, T. T., and Zhang, R. J.: Characterization and source apportionment of aerosol light extinction in Chengdu, southwest China, Atmos. 585 Environ., 95, 552–562, https://doi.org/10.1016/j.atmosenv.2014.07.017, 2014.

Tao, J., Zhang, L. M., Gao, J., Wang, H., Chai, F. H., and Wang, S. L: Aerosol chemical composition and light scattering during a winter season in Beijing, Atmos. Environ., 110, 36–44, https://doi.org/10.1016/j.atmosenv.2015.03.037, 2015.

Tian, H. Z., Lu, L., Hao, J. M., Gao, J. J., Cheng, K., Liu, K. Y., Qiu, P. P., and Zhu, C. Y.: A review of key hazardous trace elements in Chinese coals: Abundance, occurrence, behavior during coal combustion and their environmental impacts, Energ. Fuel., 27, 601–614, https://doi.org/10.1021/ef3017305, 2013.

Tian, J., Wang, Q. Y., Han, Y. M., Ye, J. H., Wang, P., Pongpiachan, S., Ni, H. Y., Zhou, Y. Q., Wang, M., Zhao, Y. Z., and Cao, J. J.: Contributions of aerosol composition and sources to particulate optical properties in a southern coastal city of China, Atmos. Res., 235, 104744, https://doi.org/ 10.1016/j.atmosres.2019.104744, 2020.

Tian, J., Wang, Q. Y., Ni, H. Y., Wang, M., Zhou, Y. Q., Han, Y. M., Shen, Z. X., Pongpiachan, S., Zhang, N. N., Zhao, Z. Z., Zhang, Q., Zhang, Y., Long, X., and Cao, J. J.: Emission characteristics of primary brown carbon absorption from biomass and coal burning: Development of an optical emission inventory for China, J. Geophys. Res.-Atmos., 124, 1879–1893, https://doi.org/10.1029/2018JD029352, 2019.

Tian, J., Wang, Q. Y., Zhang, Y., Yan, M. Y., Liu, H. K., Zhang, N. N., Ran, W. K., and Cao, J. J.: Impacts of primary emissions and secondary aerosol formation on air pollution in an urban area of China during the COVID-19 lockdown, Environ. Int., 150, 106426, https://doi.org/10.1016/j.envint.2021.106426, 2021.

Ulbrich, I. M., Canagaratna, M. R., Zhang, Q., Worsnop, D. R., and Jimenez, J. L.: Interpretation of organic components from Positive Matrix Factorization of aerosol mass spectrometric data, Atmos. Chem. Phys., 9, 2891–2918, https://doi.org/10.5194/acp-9-2891-2009, 2009.

Wang, J. F., Ye, J. H., Zhang, Q., Zhao, J., Wu, Y. Z., Li, J. Y., Liu, D. T., Li, W. J., Zhang, Y. G., Wu, C., Xie, C. H., Qin, Y. M., Lei, Y. L., Huang, X. P., Guo, J. P., Liu, P. F., Fu, P. Q., Li, Y. J., Lee, H. C., Choi, H., Zhang, J., Liao, H., Chen, M. D., Sun, Y. L., Ge, X. L., Martin, S. T., and Jacob, D. J.: Aqueous production of secondary organic aerosol from fossil-fuel emissions in winter Beijing haze, P. Natl. Acad. Sci. USA., 118, e2022179118, https://doi.org/10.1073/pnas.2022179118, 2021.

Wang, P., Cao, J. J., Shen, Z. X., Han, Y. M., Lee, S. C., Huang, Y., Zhu, C. S., Wang, Q. Y., Xu, H. M., and Huang, R. J.: Spatial and seasonal variations of $PM_{2.5}$ mass and species during 2010 in Xi'an, China, Sci. Total Environ., 508, 477–487, https://doi.org/10.1016/j.scitotenv.2014.11.007, 2015.

Wang, P.F., Chen, K.Y., Zhu, S.Q., Wang, P., and Zhang, H.L.: Severe air pollution events not avoided by reduced anthropogenic activities during COVID-19 outbreak, Resour. Conserv. Recycl., 158, 104814, https://doi.org/10.1016/j.resconrec.2020.104814, 2020a.

Wang, Q. Y., Liu, H. K., Wang, P., Dai, W. T., Zhang, T., Zhao, Y. Z., Tian, J., Zhang, W. Y., Han, Y. M., and Cao, J. J.: Optical source apportionment and radiative effect of light-absorbing carbonaceous aerosols in a tropical marine monsoon climate zone: the importance of ship emissions, Atmos. Chem. Phys., 20, 15537–15549, https://doi.org/10.5194/acp-20-15537-2020, 2020b.

Wang, X., Heald, C. L., Ridley, D. A., Schwarz, J. P., Spackman, J. R., Perring, A. E., Coe, H., Liu, D., and Clarke, A. D.: Exploiting simultaneous observational constraints on mass and absorption to estimate the global direct radiative forcing of black carbon and brown carbon, Atmos. Chem. Phys., 14, 17527–17583, https://doi.org/10.5194/acp-14-10989-2014, 2014.

Wang, Y. C., Yuan, Y., Wang, Q. Y., Liu, C. G., Zhi, Q., and Cao, J. J.: Changes in air quality related to the control of coronavirus in China: Implications for traffic and industrial emissions, Sci. Total Environ., 731, 139133, https://doi.org/10.1016/j.scitotenv.2020.139133, 2020c.

Weber, J., Shin, Y. M., Staunton Sykes, J., Archer-Nicholls, S., Abraham, N. L., and Archibald, A. T.: Minimal climate impacts from short-lived climate forcers following emission reductions related to the COVID-19 pandemic, Geophys. Res. Lett., 47, e2020GL090326. https://doi.org/10.1029/2020GL090326, 2020.

Wood, S. N.: Generalized additive models: An introduction with R (2nd ed), CRC press, 496pp, https://doi.org/10.1201/9781315370279, 2017.

Wood, S. N.: Stable and efficient multiple smoothing parameter estimation for generalized additive models, J. Am. Stat. Assoc., 99, 673–686, https://doi.org/10.1198/016214504000000980, 2004.

Wu, J. R., Bei, N. F., Li, X., Cao, J. J., Feng, T., Wang, Y. C., Tie, X. X., and Li, G. H.: Widespread air pollutants of the North China Plain during the Asian summer monsoon season: a case study, Atmos. Chem. Phys., 18, 8491–8504, https://doi.org/10.5194/acp-18-8491-2018, 2018.

Xie, M. J., Chen, X., Holder, A. L., Hays, M. D., Lewandowski, M., Offenberg, J. H., Kleindienst, T. E., Jaoui, M., and Hannigan, M. P.: Light absorption of organic carbon and its sources at a southeastern U.S. location in summer, Environ. Pollut., 244, 38–46, https://doi.org/10.1016/j.envpol.2018.09.125, 2019.

Xu, H. M., Cao, J. J., Ho, K. F., Ding, H., Han, Y. M., Wang, G. H., Chow, J. C., Watson, J. G., Khol, S. D., Qiang, J., Li, W. T.: Lead concentrations in fine particulate matter after the phasing out of leaded gasoline in Xi'an, China, Atmos. Environ., 46, 217–224, https://doi.org/10.1016/j.atmosenv.2011.09.078, 2012.

Xu, L., Zhang, J., Sun, X., Xu, S. C., Shan, M., Yuan, Q., Liu, L., Du, Z. H., Liu, D. T., Xu, D., Song, C. B., Liu, B. W., Lu, G. D., Shi, Z. B., and Li, W. J.: Variation in concentration and sources of black carbon in a megacity of China during the COVID-19 pandemic, Geophys. Res. Lett., 47, e2020GL090444, https://doi.org/10.1029/2020GL090444, 2020a.

Xu, W. Q., Sun, Y. L., Chen, C., Du, W., Han, T. T., Wang, Q. Q., Fu, P. Q., Wang, Z. F., Zhao, X. J., Zhou, L. B., Ji, D. S., Wang, P. C., and Worsnop, D. R.: Aerosol composition, oxidation properties, and sources in Beijing: results from the 2014 Asia-Pacific Economic Cooperation summit study, Atmos. Chem. Phys., 15, 13681–13698, https://doi.org/10.5194/acp-15-13681-2015, 2015.

Xu, W. Y., Kuang, Y., Bian, Y. X., Liu, L., Li, F., Wang, Y. Q., Xue, B., Luo, B., Huang, S., Yuan, B., Zhao, P. S., and Shao, M.: Current challenges in visibility improvement in southern China, Environ. Sci. Technol. Lett., 7, 395–401, https://doi.org/10.1021/acs.estlett.0c00274, 2020b.

Yao, H., Song, Y., Liu, M. X., Archer-Nicholls, S., Lowe, D., McFiggans, G., Xu, T. T., Du, P., Li, J. F., Wu, Y. S., Hu, M., Zhao, C., and Zhu, T.: Direct radiative effect of carbonaceous aerosols from crop residue burning during the summer harvest season in East China, Atmos. Chem. Phys., 17, 5205–5219, https://doi.org/10.5194/acp-17-5205-2017, 2017.

Yao, L. Q., Kong, S. F., Zheng, H., Chen, N., Zhu, B., Xu, K., Cao, W. X., Zhang, Y., Zheng, M. M., Cheng, Y., Hu, Y., Zhang, Z. X., Yan, Y. Y., Liu, D. T., Zhao, T. L., Bai, Y. Q., and Qi, S. H.: Co-benefits of reducing $PM_{2.5}$ and improving visibility by COVID-19 lockdown in Wuhan, NPJ Clim. Atmos. Sci., 4, 40, https://doi.org/10.1038/s41612-021-00195-6, 2021.

Yao, M. S., Zhang, L., Ma, J. X., and Zhou, L.: On airborne transmission and control of SARS-Cov-2, Sci. Total Environ., 731, 139178, https://doi.org/10.1016/j.scitotenv.2020.139178, 2020.

Yu, Y. Y., He, S. Y., Wu, X. L., Zhang, C., Yao, Y., Liao, H., Wang, Q. G., and Xie, M. J.: $PM_{2.5}$ elements at an urban site in Yangtze River Delta, China: High time-resolved measurement and the application in source apportionment, Environ. Pollut., 253, 1089–1099, https://doi.org/10.1016/j.envpol.2019.07.096, 2019.

Zhang, R., Jing, J., Tao, J., Hsu, S. C., Wang, G., Cao, J., Lee, C. S. L., Zhu, L., Chen, Z., Zhao, Y., and Shen, Z.: Chemical characterization and source apportionment of $PM_{2.5}$ in Beijing: seasonal perspective, Atmos. Chem. Phys., 13, 7053–7074, https://doi.org/10.5194/acp-13-7053-2013, 2013a.

Zhang, R. Y., Wang, G. H., Guo, S., Zamora, M. L., Ying, Q., Lin, Y., Wang, W. G., Hu, M., and Wang, Y.: Formation of urban fine particulate matter, Chem. Rev., 115, 3803–3855, https://doi.org/10.1021/acs.chemrev.5b00067, 2015.

Zhang, Q., Shen, Z. X., Zhang, L. M., Zeng, Y. L., Ning, Z., Zhang, T., Lei, Y. L., Wang, Q. Y., Li, G. H., Sun, J., Westerdahl, D., Xu, H. M., and Cao, J. J.: Investigation of primary and secondary particulate brown carbon in two Chinese cities of Xi'an and Hong Kong in wintertime, Environ. Sci. Technol., 54, 3803–3813, https://doi.org/10.1021/acs.est.9b05332, 2020.

Zhang, Y. M., Sun, J. Y., Zhang, X. Y., Shen, X. J., Wang, T. T., and Qin, M. K.: Seasonal characterization of components and size distributions for submicron aerosols in Beijing, Sci. China-Earth Sci., 56, 890–900, https://doi.org/10.1007/s11430-012-4515-z, 2013b.

Zhao, P. S., Feng, Y. C., Tan, Z., and Wu, J. H.: Characterizations of resuspended dust in six cities of North China, Atmos. Environ., 40, 5807–5814, https://doi.org/10.1016/j.atmosenv.2006.05.026, 2006.

Zhao, Y. B., Zhang, K., Xu, X. T., Shen, H. Z., Zhu, X., Zhang, Y. X., Hu, Y. T., and Shen, G. F.: Substantial changes in nitrogen dioxide and ozone after excluding meteorological impacts during the COVID-19 outbreak in mainland China, Environ. Sci. Technol. Lett., 7, 402–408, https://doi.org/10.1021/acs.estlett.0c00304, 2020.

Zheng, B., Huo, H., Zhang, Q., Yao, Z. L., Wang, X. T., Yang, X. F., Liu, H., and He, K. B.: High-resolution mapping of vehicle emissions in China in 2008, Atmos. Chem. Phys., 14, 9787–9805, https://doi.org/10.5194/acp-14-9787-2014, 2014.

Zheng, B., Tong, D., Li, M., Liu, F., Hong, C. P., Geng, G. N., Li, H. Y., Li, X., Peng, L. Q., Qi, J., Yan, L., Zhang, Y. X., Zhao, H. Y., Zheng, Y. X., He, K. B., and Zhang, Q.: Trends in China's anthropogenic emissions since 2010 as the consequence of clean air actions, Atmos. Chem. Phys., 18, 14095–14111, https://doi.org/10.5194/acp-18-14095-2018, 2018.

Zheng, H., Kong, S. F., Chen, N., Yan, Y. Y., Liu, D. T., Zhu, B., Xu, K., Cao, W. X., Ding, Q. Q., Lan, B., Zhang, Z. X., Zheng, M. M., Fan, Z. W., Cheng, Y., Zheng, S. R., Yao, L. Q., Bai, Y. Q., Zhao, T. L., and Qi, S. H.: Significant changes in the chemical compositions and sources of $PM_{2.5}$ in Wuhan since the city lockdown as COVID-19. Sci. Total Environ., 739, 140000, https://doi.org/10.1016/j.scitotenv.2020.140000, 2020.

Zhou, Y. Q., Wang, Q. Y., Huang, R. J., Liu, S. X., Tie, X. X., Su, X. L., Niu, X. Y., Zhao, Z. Z., Ni, H. Y., Wang, M., Zhang, Y. G., and Cao, J. J.: Optical properties of aerosols and implications for radiative effects in Beijing during the Asia-Pacific Economic Cooperation (APEC) Summit 2014, J. Geophys. Res.-Atmos., 122, 10119–10132, https://doi.org/10.1002/2017jd026997, 2017.

Zhu, W. F., Zhou, M., Cheng, Z., Yan, N. Q., Huang, C., Qiao, L. P., Wang, H. L., Liu, Y, C., Lou, S. R., and Guo, S.: Seasonal variation of aerosol compositions in Shanghai, China: Insights from particle aerosol mass spectrometer observations, Sci. Total Environ., 771, 144948, https://doi.org/10.1016/j.scitotenv.2021.144948, 2021.

Zotter, P., Herich, H., Gysel, M., El-Haddad, I., Zhang, Y., Močnik, G., Hüglin, C. Baltensperger, U., Szidat, S., and Prévôt, A. S. H.: Evaluation of the absorption Ångström exponents for traffic and wood burning in the Aethalometer-based source apportionment using radiocarbon measurements of ambient aerosol, Atmos. Chem. Phys., 17, 4229–4249, https://doi.org/10.5194/acp-17-4229-2017, 2017.

Table 1. Summary of optical coefficients and chemical species in Xi'an observed in the entire campaign, normal period (January 1st to 23rd, 2020), and COVID-19 lockdown period (January 27th to February 7th, 2020).

Parameters[*]	Entire campaign	Normal period	COVID-19 lockdown period	Change ratio[**]
Optical coefficients				
b_{scat}	623.2 ±248.3	688.1 ±261.4	498.4 ±159.0	27.6%
b_{abs}	72.6 ±42.1	86.6 ±43.0	45.9 ±22.9	47.0%
b_{ext}	695.8 ±285.3	774.7 ±298.1	544.3 ±179.4	29.7%
SSA	0.90 ±0.03	0.89 ±0.03	0.92 ±0.02	-3.2%
Chemical species				
$PM_{2.5}$	116.4 ±56.3	134.4 ±56.9	81.8 ±34.9	39.1%
NH_4NO_3	33.1 ±17.3	40.2 ±16.4	19.5 ±8.8	51.6%
$(NH4)_2SO_4$	8.3 ±4.6	9.5 ±4.9	5.9 ±2.5	38.1%
fine soil	11.8 ±8.0	15.8 ±7.2	4.3 ±1.9	72.5%
BC	4.4 ±2.6	5.4 ±2.6	2.7 ±1.3	50.6%
POA	18.3 ±12.4	20.9 ±12.7	13.4 ±10.1	35.8%
LO-OOA	7.6 ±5.8	8.6 ±6.4	5.6 ±3.7	34.7%
MO-OOA	11.1 ±4.5	12.0 ±4.8	9.5 ±3.3	20.9%

[*]The units for b_{scat}, b_{abs}, b_{ext} are Mm^{-1}; SSA is dimensionless; The units of chemical species are $\mu g\ m^{-3}$.

710 [**]Change ratio = ([Normal period] − [COVID-19 lockdown period])/[Normal period]×100%.

Table 2. Estimated MSEs and MAEs (m^2 g^{-1}) of individual chemical components during normal and COVID-19 lockdown periods.

Components	Normal period		COVID-19 lockdown period	
	MSE	MAE	MSE	MAE
NH_4NO_3	3.74 ±0.18		3.23 ±0.18	
$(NH_4)_2SO_4$	7.35 ±0.25		4.78 ±0.35	
fine soil	2.46 ±0.35		3.39 ±0.79	
BC		15.00		13.27
POA	3.90 ±0.18	0.25 ±0.01	3.48 ±0.16	0.29 ±0.01
LO-OOA	8.62 ±0.27	0.27 ±0.02	9.87 ±0.35	0.59 ±0.03
MO-OOA	9.87 ±0.45	/	12.89 ±0.55	0.31 ±0.04

[*]MAE of MO-OOA during the normal period was negative (near zero) and not listed in the table.
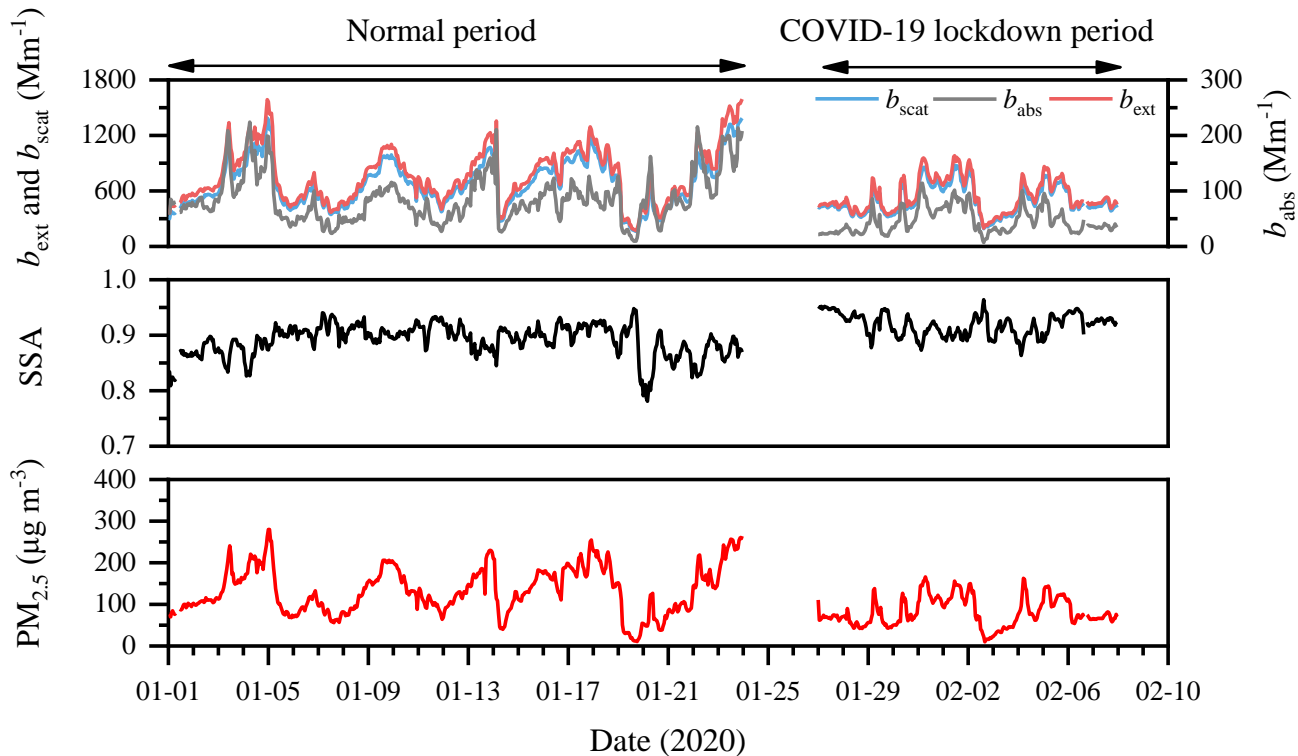
715

Figure captions:

Figure 1. Hourly variations of light scattering (b_{scat}), absorption (b_{abs}), and extinction (b_{ext}) coefficients, single scattering albedo (SSA), and PM$_{2.5}$ mass concentrations in Xi'an during the normal (January 1st to 23rd, 2020) and COVID-19 lockdown (January 27th to February 7th, 2020) periods.

Figure 2. Variations of single scattering albedo (SSA) as a function of (a) secondary inorganic aerosol (SIA = NH$_4$NO$_3$ + (NH$_4$)$_2$SO$_4$)/PM$_{2.5}$, (b) secondary organic aerosol (SOA = LO-OOA + MO-OOA)/OA, and (c) LO-OOA/MO-OOA ratios during the normal and COVID-19 lockdown periods.

Figure 3. Time series of the measured and GAM-predicted light extinction coefficient (b_{ext}) for the model data, test data, and forecast data.

Figure 4. Contributions of NH$_4$NO$_3$, (NH$_4$)$_2$SO$_4$, fine soil, BC, POA, LO-OOA, and MO-OOA to the reconstructed chemical light extinction coefficient (b_{ext}) during the normal and COVID-19 lockdown periods.

Figure 5. (a) Profiles and (b) time series plots of the resolved source factors in the six-factor solution, including traffic-related emission, biomass burning, coal combustion, fugitive dust, nitrate plus SOA source, and sulfate plus SOA source. The columns in each factor are the profile that displays the relative relation of absolute values of variables. The red dot represents the explained variation of species for different factors. The corresponding time trends of chemical tracers are also shown.

Figure 6. Contributions of six resolved sources to the modeled source light extinction coefficient (b_{ext}) during the normal and COVID-19 lockdown periods, including traffic-related emission, biomass burning, coal combustion, fugitive dust, nitrate plus SOA source, and sulfate plus SOA source.

Figure 7. Time series of PM$_{2.5}$ mass concentration, the light extinction coefficient (b_{ext}) of chemical species, and the b_{ext} from six resolved sources during the lockdown period. Pie charts depicting the average fractional contributions of chemical species and sources to b_{ext} during the PM$_{2.5}$ rising stages, which were marked in light gray.

Figure 8. Direct radiative effect (DRE) of aerosol from traffic-related emission, biomass burning, coal combustion, fugitive dust, nitrate plus SOA source, and sulfate plus SOA source at the earth's surface, the top of the atmosphere, and in the atmosphere during the normal (a) and COVID-19 lockdown (b) periods.

Figure 1. Hourly variations of light scattering (b_{scat}), absorption (b_{abs}), and extinction (b_{ext}) coefficients, single scattering albedo (SSA), and PM$_{2.5}$ mass concentrations in Xi'an during the normal (January 1st to 23rd, 2020) and COVID-19 lockdown (January 27th to February 7th, 2020) periods.
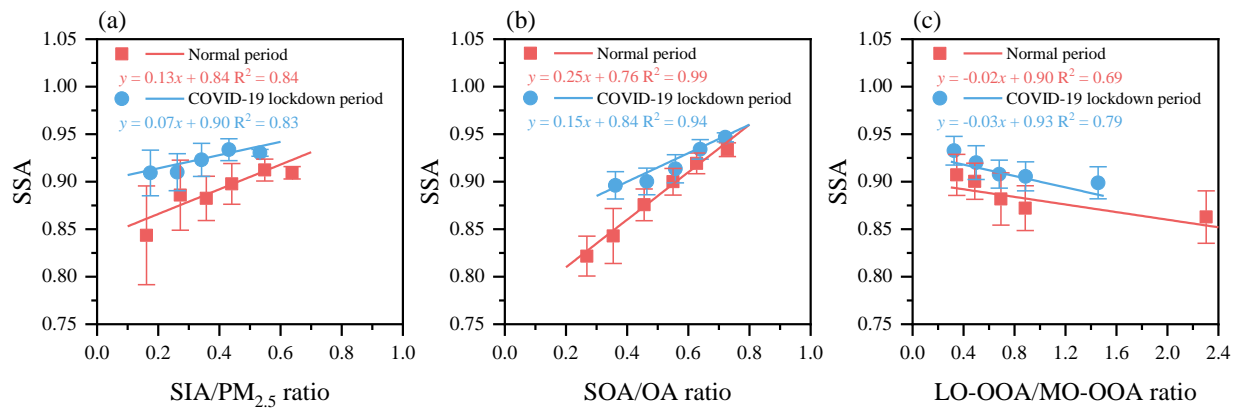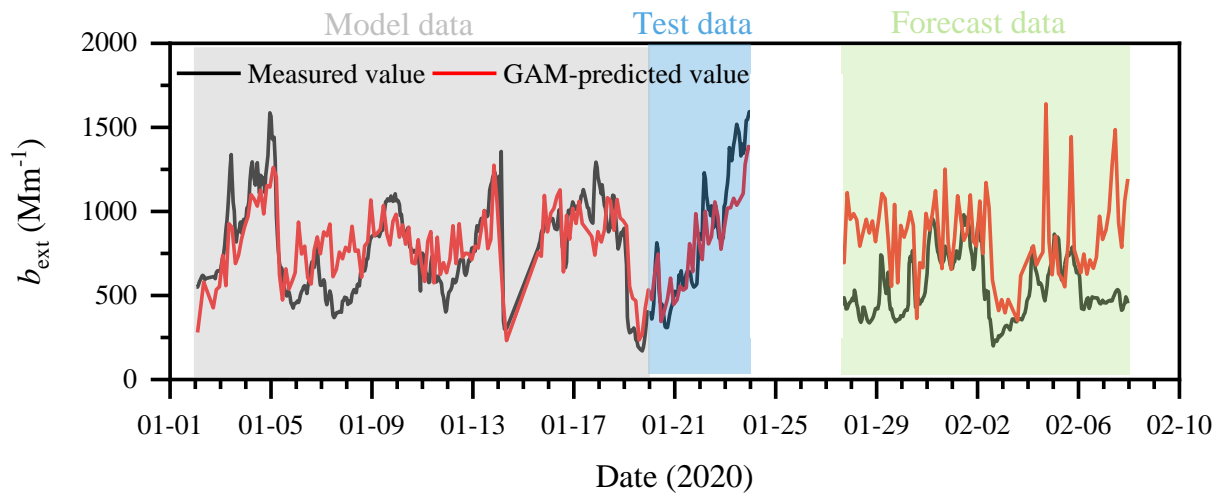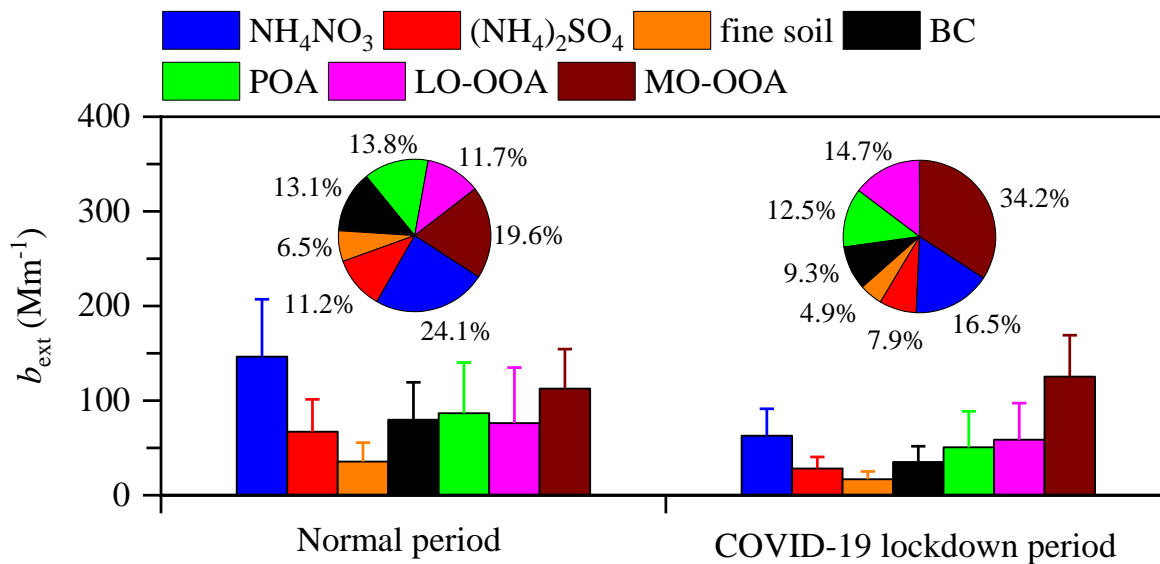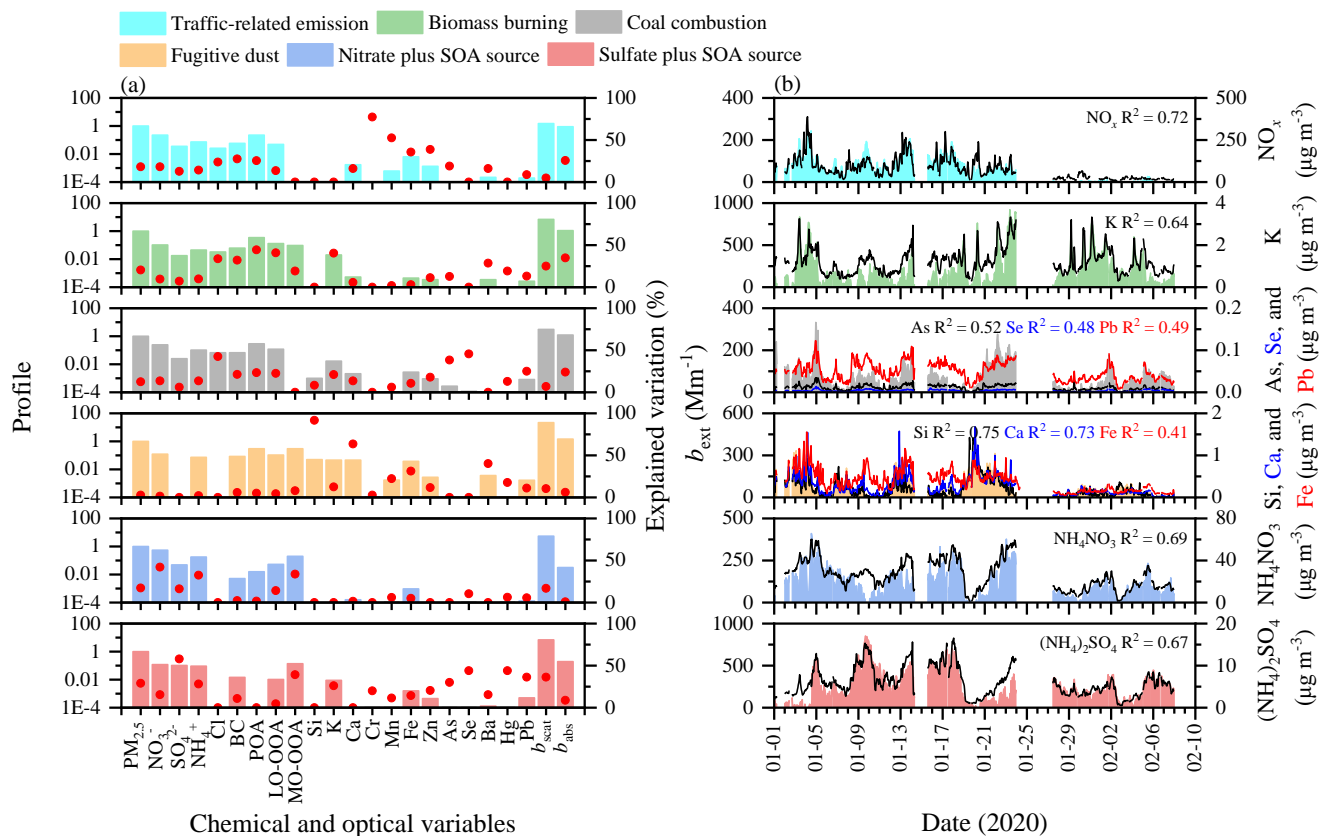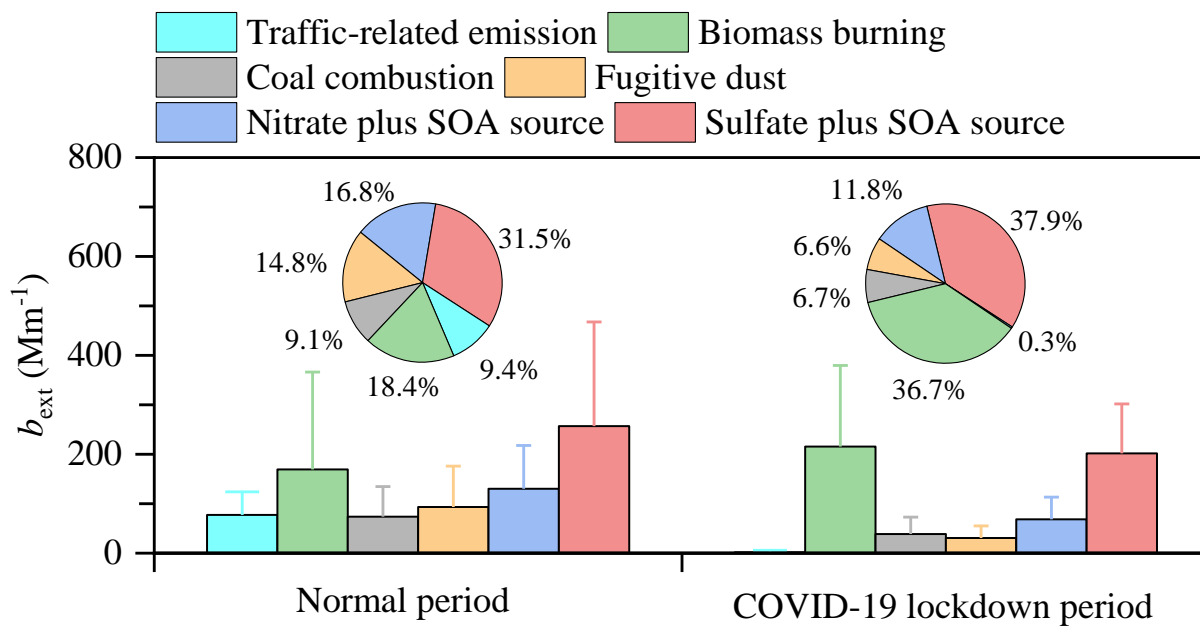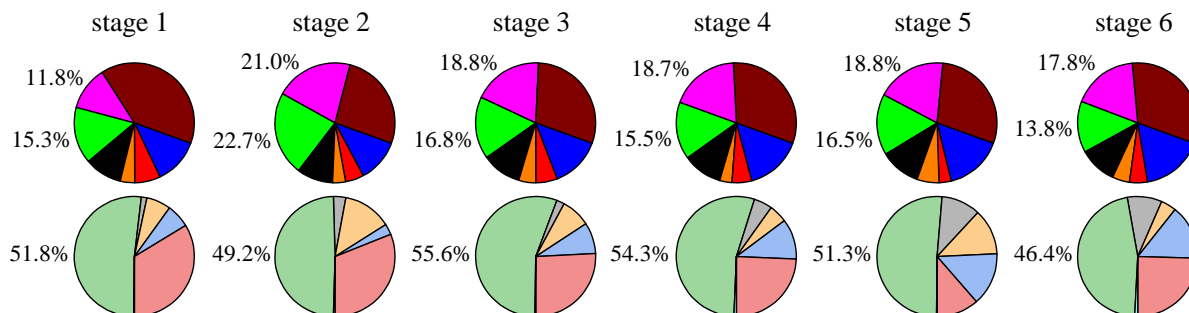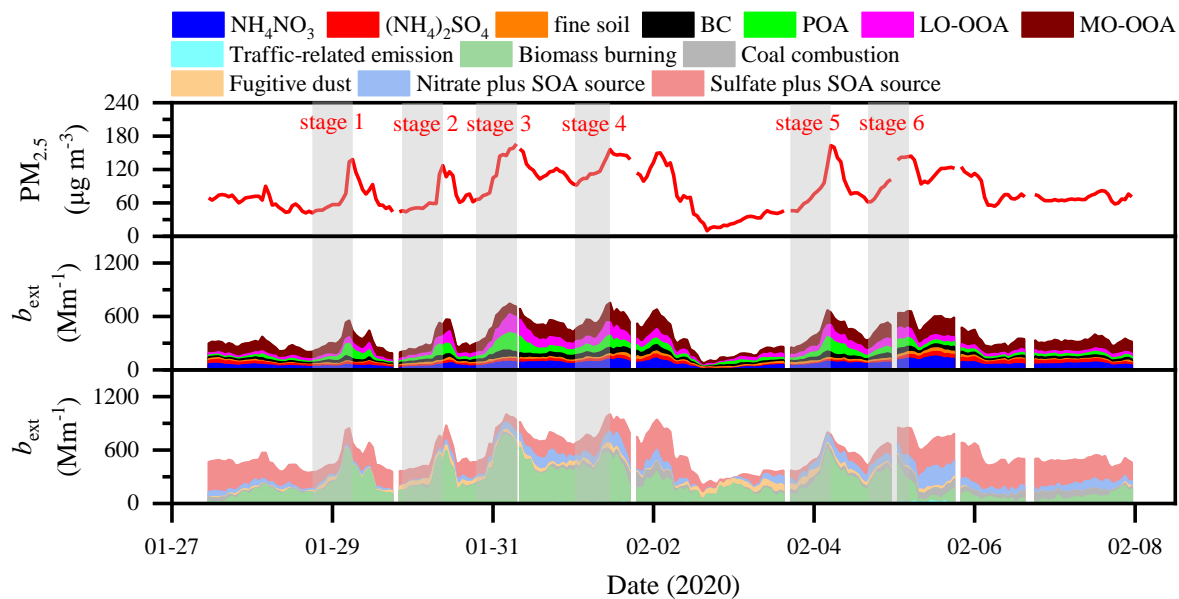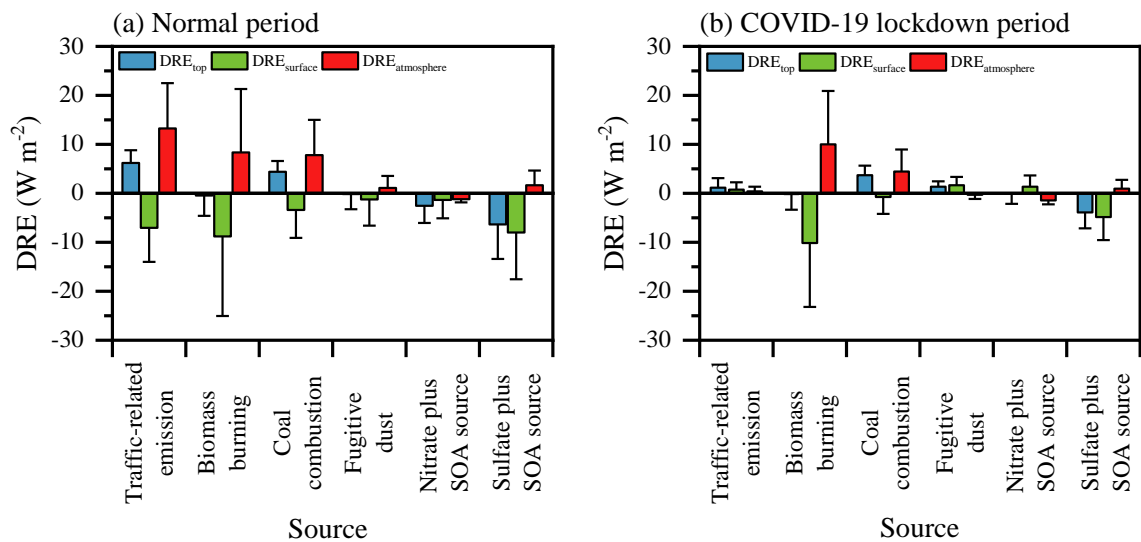
Figure 2. Variations of single scattering albedo (SSA) as a function of (a) secondary inorganic aerosol (SIA = NH_4NO_3 + $(NH_4)_2SO_4$)/$PM_{2.5}$, (b) secondary organic aerosol (SOA = LO-OOA + MO-OOA)/OA, and (c) LO-OOA/MO-OOA ratios during the normal and COVID-19 lockdown periods.

750

Figure 3. Time series of the measured and GAM-predicted light extinction coefficient (b_{ext}) for the model data, test data, and forecast data.

Figure 4. Contributions of NH_4NO_3, $(NH_4)_2SO_4$, fine soil, BC, POA, LO-OOA, and MO-OOA to the reconstructed chemical light extinction coefficient (b_{ext}) during the normal and COVID-19 lockdown periods.

Figure 5. (a) Profiles and (b) time series plots of the resolved source factors in the six-factor solution, including traffic-related emission, biomass burning, coal combustion, fugitive dust, nitrate plus SOA source, and sulfate plus SOA source. The columns in each factor are the profile that displays the relative relation of absolute values of variables. The red dot represents the explained variation of species for different factors. The corresponding time trends of chemical tracers are also shown.

765 **Figure 6.** Contributions of six resolved sources to the modeled source light extinction coefficient (b_{ext}) during the normal and COVID-19 lockdown periods, including traffic-related emission, biomass burning, coal combustion, fugitive dust, nitrate plus SOA source, and sulfate plus SOA source.

Figure 7. Time series of PM$_{2.5}$ mass concentration, the light extinction coefficient (b_{ext}) of chemical species, and the b_{ext} from six resolved sources during the lockdown period. Pie charts depicting the average fractional contributions of chemical species and sources to b_{ext} during the PM$_{2.5}$ rising stages, which were marked in light gray.

Figure 8. Direct radiative effect (DRE) of aerosol from traffic-related emission, biomass burning, coal combustion, fugitive dust, nitrate plus SOA source, and sulfate plus SOA source at the earth's surface, the top of the atmosphere, and in the atmosphere during the normal (a) and COVID-19 lockdown (b) periods.

Measurement report: The importance of biomass burning in light extinction and direct radiative effect of urban aerosol during the COVID-19 lockdown in Xi'an, China

Jie Tian[1,2], Qiyuan Wang[1,2,3], Huikun Liu[1], Yongyong Ma[4], Suixin Liu[1,2], Yong Zhang[1], Weikang Ran[1], Yongming Han[1,2,3], and Junji Cao[5]

[1]State Key Laboratory of Loess and Quaternary Geology, Institute of Earth Environment, Chinese Academy of Sciences, Xi'an 710061, China
[2]CAS Center for Excellence in Quaternary Science and Global Change, Xi'an 710061, China
[3]National Observation and Research Station of Regional Ecological Environment Change and Comprehensive Management in the Guanzhong Plain, Shaanxi, Xi'an 710061, China
[4]Meteorological Institute of Shaanxi Province, Xi'an 710015, China
[5]Institute of Atmospheric Physics, Chinese Academy of Sciences, Beijing 100029, China

Correspondence: Qiyuan Wang (wangqy@ieecas.cn) and Junji Cao (jjcao@mail.iap.ac.cn)

16   **Text S1.** Absorption Ångström exponent method

17   In this study, aerosol light absorption coefficient (b_{abs}) at wavelengths of $\lambda = 370$ nm, 470 nm, 520 nm,

18   590 nm, 660 nm, and 880 nm were measured by a newly developed Aethalometer (model AE33, Magee

19   Scientific, Berkeley, CA, USA). The Absorption Ångström exponent (AAE) describes the wavelength

20   dependence of aerosol light absorption and can be calculated according to power law fitting b_{abs} at

21   wavelengths of 370 nm to 880 nm (Moosmüller et al., 2011) as below:

22    $$b_{abs}(\lambda) \sim \lambda^{-AAE} \tag{1}$$

23   Through the AAE method (Lack and Langridge, 2013), the mass absorption efficiency (MAE) of black

24   carbon (BC) at 520 nm can be obtained as follows:

25    $$b_{abs}(520 \text{ nm}) = b_{abs\text{-}BC}(520 \text{ nm}) + b_{abs\text{-}BrC}(520 \text{ nm}) \tag{2}$$

26    $$b_{abs\text{-}BC}(520 \text{ nm}) = b_{abs\text{-}BC}(880 \text{ nm}) \times \left(\frac{520}{880}\right)^{-AAE_{BC}} \tag{3}$$

27    $$MAE_{BC}(520 \text{ nm}) = \frac{b_{abs\text{-}BC}(520 \text{ nm})}{[BC]} \tag{4}$$

28   where b_{abs}-BC and b_{abs}-BrC in Mm^{-1} are the light absorption coefficients caused by BC and brown

29   carbon (BrC), respectively; AAE_{BC} is the AAE caused by the BC particle, which can vary from 0.8 to

30   1.4 due to core size, coating materials, and mixing state (Lack and Cappa, 2010; Lack and Langridge,

31   2013). The linear relationship between the AAEs and the mass concentration ratios of organic aerosol

32   (OA) to BC is investigated to find the realistic AAE_{BC} during the normal and lockdown periods (Figure

33   S12) (Yuan et al., 2016); and [BC] is the mass concentration of BC in μg m^{-3}.

44   **Text S2.** Uncertainty of the element concentration

45   Considering the element concentration measured by the Xact 625 ambient metals monitor with a 1-hour

46   sampling interval, the uncertainty of the element concentration (u_e) inputting into the receptor model

47   was estimated as follows (Norris et al., 2014):

48    $$u_e = \sqrt{(c_e \times 10\%)^2 + (0.5 \times MDL)^2}, \text{ for } c_e > MDL \qquad (5)$$

49    $$u_e = \frac{5}{6} \times MDL, \text{ for } c_e \leq MDL \qquad (6)$$

50   where c_e is the concentration of the element; 10% is the default analytical relative error (Rai et al., 2020);

51   and MDL represents the method detection limit of the element.

52   **Text S3.** Diagnostics of HERM solutions

53   In this study, factor numbers from two to eight were selected to run in the HERM software. Each factor

54   solution was performed with completely unconstrained profiles at twenty different seeds to explore the

55   possible sources. Detailed information on how the most interpretable factors were selected is presented

56   below.

57   As shown in Figure S2, the values of Q/Q_{exp} (> 1) decreased as the factor numbers increased. The large

58   Q/Q_{exp} values in two- (21.10 ±0.03) and three-factor (12.29 ±0.01) solutions indicated too few factors

59   were resolved. In the four-factor solution (Figure S3), Factor 2 identified as biomass burning was

60   characterized by high explained variations (EV) values of POA (56%), LO-OOA (54%), BC (43%), Cl

61   (55%). Factor 3 was regarded as fugitive dust due to significant EV values of Si (100%), Ca (68%), and

62   Fe (35%). For the Factor 4 assigned to the secondary source, EV values of NO_3^-, SO_4^{2-}, NH_4^+, and MO-

63   OOA were larger than 30%. It is noted that Factor 1 was associated with the traffic-like source because

64   b_{ext} from this source showed a moderate correlation with NO_x, a tracer of fresh motor vehicle exhaust

65   emission ($R^2 = 0.58$). However, the high EV values of some specific elements (e.g., As (44%) and Se

66   (31%)) in this factor indicated the possible mixture of other fossil fuel sources (e.g., coal combustion).

67   When five factors were resolved, except traffic-like source (Factor 1), biomass burning (Factor 2), and

68   fugitive dust (Factor 3), the secondary source was split into nitrate plus SOA (Factor 4) and sulfate plus

69   SOA (Factor 5) sources (Figure S4). The increase to six-factor solution (Figure S5) showed well

70   separation of traffic-related emission (Factor 1) and coal combustion (Factor 3). A stronger correlation

71   between b_{ext} from traffic-related emission and NO_x ($R^2 = 0.72$) was found compared to traffic-like

72   factors resolved in four– and five- factor solutions ($R^2 = 0.58$). As shown in Figures S6 and S7, further

73   investigations of unconstrained profile solutions with seven and eight factors resulted in factor split. The

74   extra split factors possibly came from biomass burning and coal combustion, mainly due to high EV

75   values of K (26–33%), or As (21%). Despite b_{ext} from coal combustion factors in seven- and eight-

76   factor solutions showed the stronger correlation with As ($R^2 = 0.63$–0.68), Se ($R^2 = 0.79$–0.86), and Pb

77   ($R^2 = 0.60$–0.67), the profiles identified coal combustion had no POA contribution. Meanwhile, the

78   values of POA in fugitive dust profiles identified in seven– and eight- factor solutions were higher than

79   1 (the reference standard of $PM_{2.5}$). It is indicated that these profiles did not match the real world.
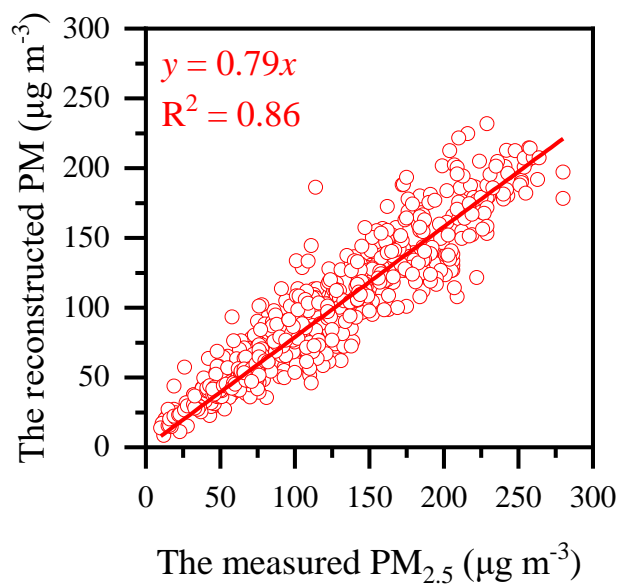
80   Therefore, as the factor solutions described above, six factors were the most interpretable in our study,

81   including traffic-related emission, biomass burning, coal combustion, fugitive dust, nitrate plus SOA

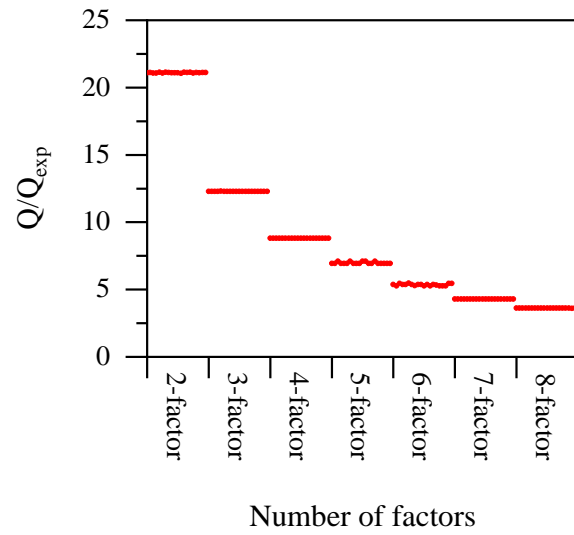82   source, and sulfate plus SOA source.
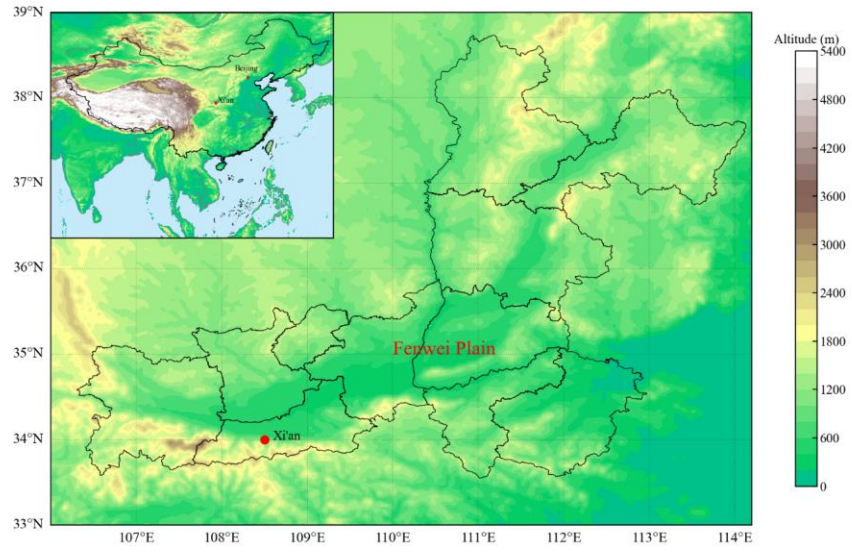
83

84   **Figure S1.** The location of the sampling site in Xi'an, China.

The reconstructed PM ($\mu g\ m^{-3}$) vs. The measured $PM_{2.5}$ ($\mu g\ m^{-3}$)

$y = 0.79x$
$R^2 = 0.86$

Figure S2. Linear relationship between the measured $PM_{2.5}$ concentration and the sum concentration of POA, LO-OOA, MO-OOA, NH_4NO_3, $(NH_4)_2SO_4$, BC, and fine soil (the sum is referred to as the reconstructed PM).

90

91 **Figure S2S3.** Values of Q/Q_{exp} for the unconstrained profile solutions with two to eight factors at twenty
92 different seeds.
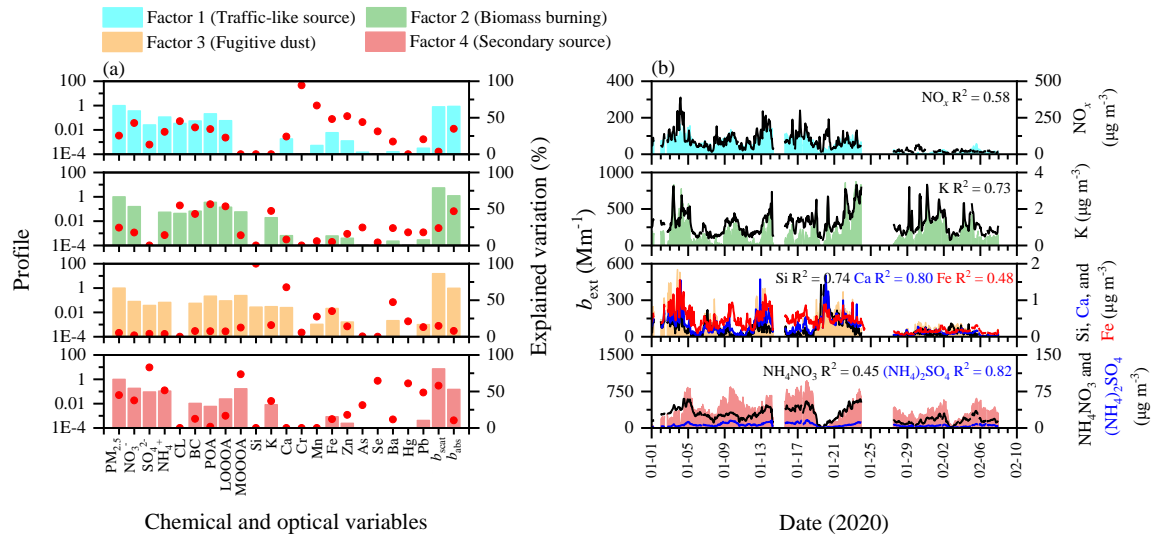
Figure S3S4. (a) Profiles and (b) time series plots of the resolved source factors in the four-factor solution. The columns in each factor are the profile that displays the relative relation of absolute values of variables. The red dot represents the explained variation of species for different factors. The corresponding time trends of chemical tracers also are shown.
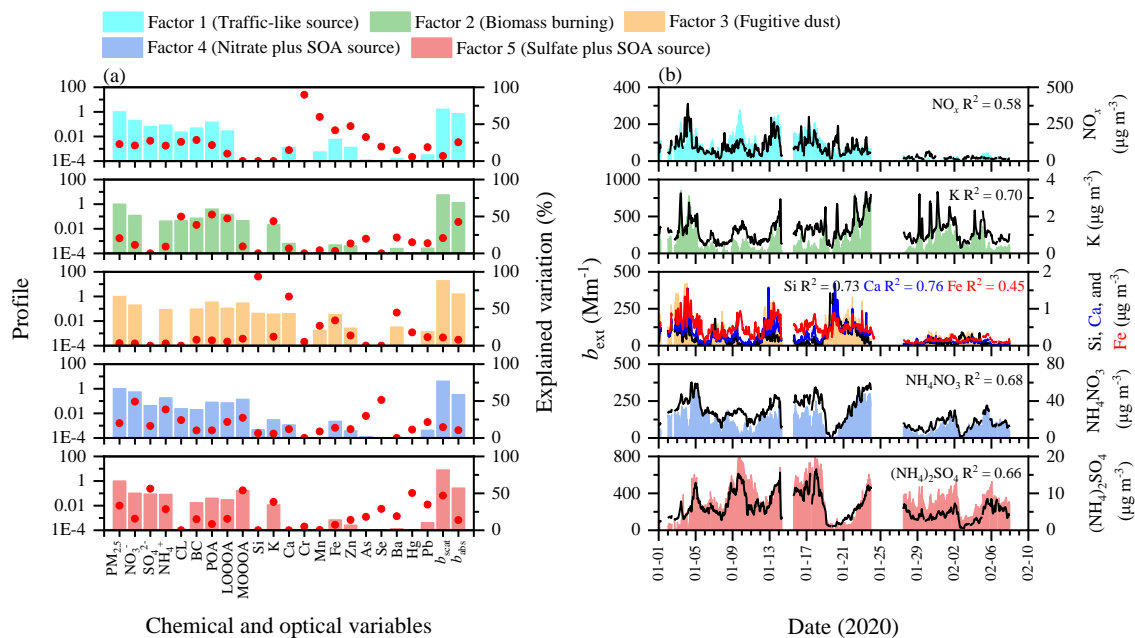
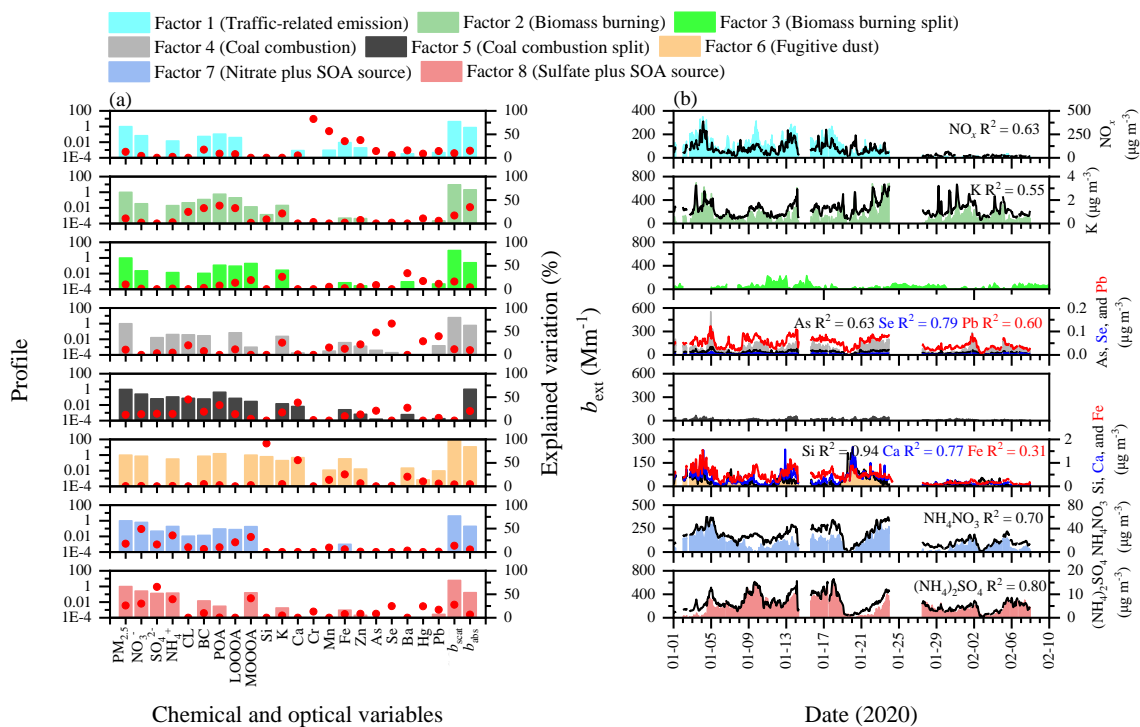Figure S4S5. (a) Profiles and (b) time series plots of the resolved source factors in the five-factor solution. The columns in each factor are the profile that displays the relative relation of absolute values of variables. The red dot represents the explained variation of species for different factors. The corresponding time trends of chemical tracers also are shown.

103
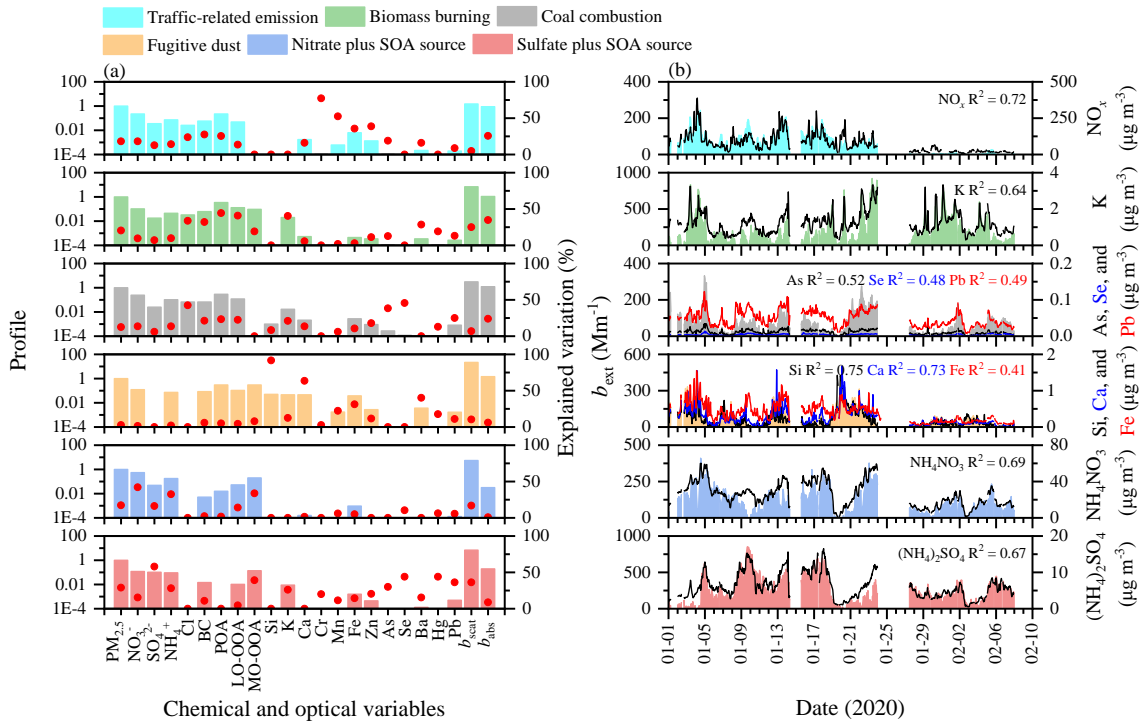
Figure S5S6. (a) Profiles and (b) time series plots of the resolved source factors in the six-factor solution. The columns in each factor are the profile that displays the relative relation of absolute values of variables. The red dot represents the explained variation of species for different factors. The corresponding time trends of chemical tracers also are shown.
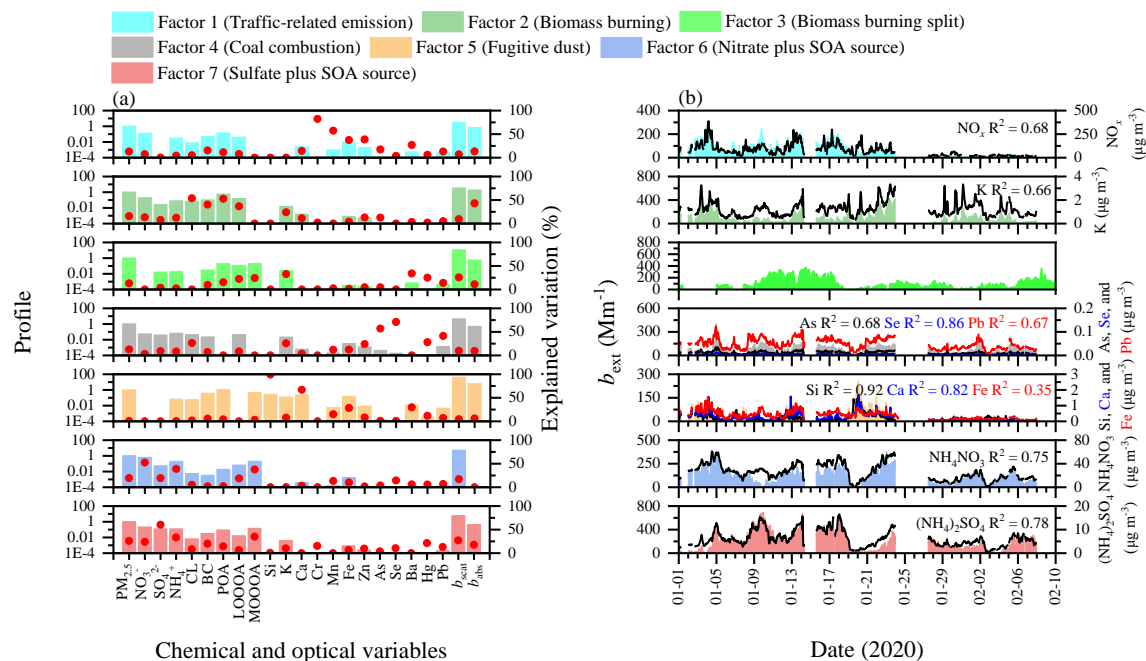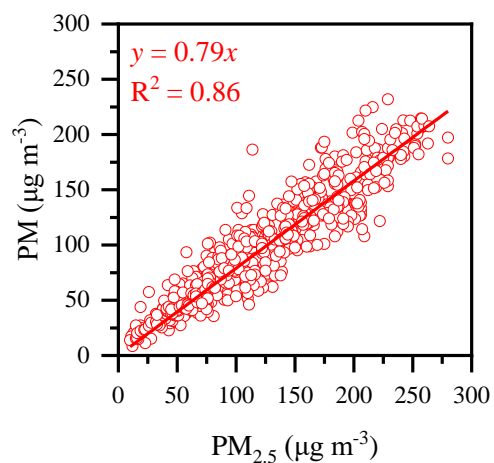
Figure ~~S6~~S7. (a) Profiles and (b) time series plots of the resolved source factors in the seven-factor solution. The columns in each factor are the profile that displays the relative relation of absolute values of variables. The red dot represents the explained variation of species for different factors. The corresponding time trends of chemical tracers also are shown.

Figure S7S8. (a) Profiles and (b) time series plots of the resolved source factors in the eight-factor
solution. The columns in each factor are the profile that displays the relative relation of absolute values
of variables. The red dot represents the explained variation of species for different factors. The
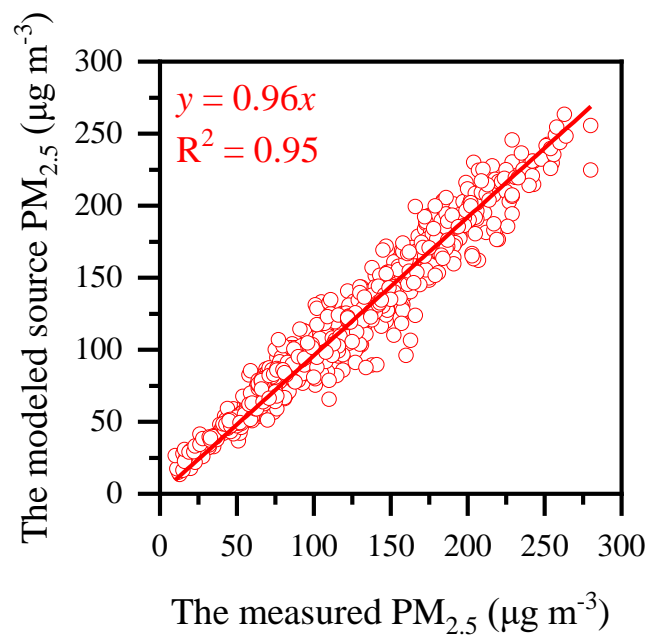corresponding time trends of chemical tracers also are shown.
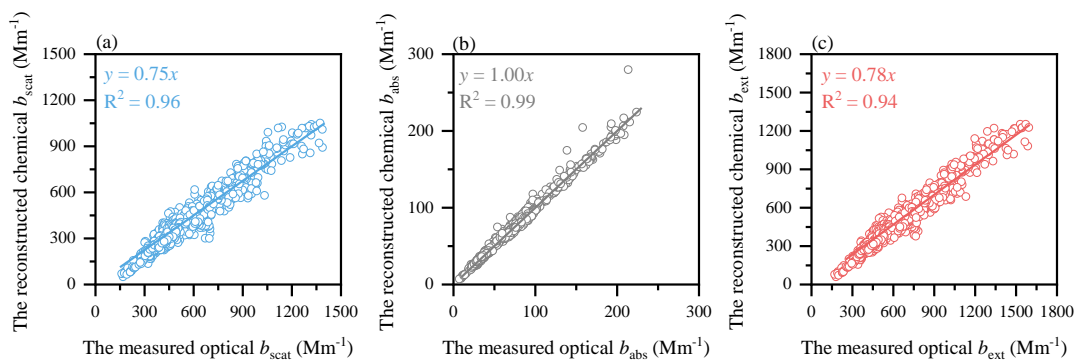
Figure S98. Linear relationships between the reconstructed chemical and the measured optical (a) b_{scat}, (b) b_{abs}, and (c) b_{ext}.

121

The figure shows a scatter plot with axis label "The modeled source PM$_{2.5}$ (μg m^{-3})" on the y-axis and "The measured PM$_{2.5}$ (μg m^{-3})" on the x-axis. Both axes range from 0 to 300. The plot contains the text:

$y = 0.96x$

$R^2 = 0.95$

128

Figure S10. Linear relationship between the modeled source and the measured PM$_{2.5}$ mass concentration. The modeled source PM$_{2.5}$ was strongly correlated linearly with the measured optical PM$_{2.5}$ ($R^2 = 0.95$, slope $= 0.96$), indicating that the six identified sources can adequately account for the variability in PM$_{2.5}$ mass concentration.

134
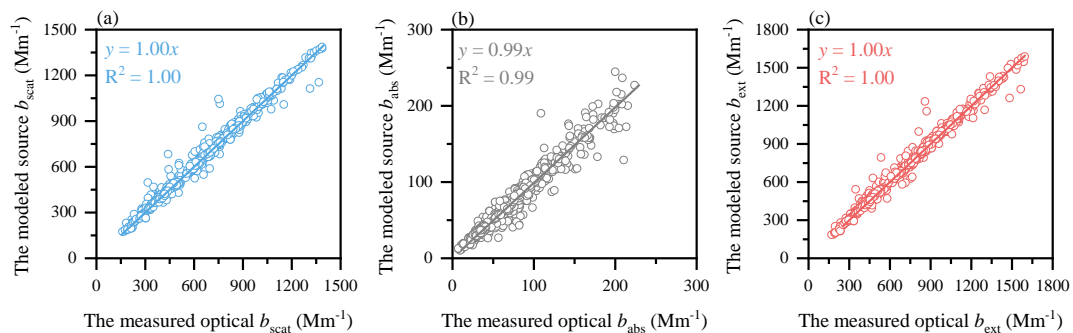
Figure S11. Linear relationships between the modeled source and the measured optical (a) b_{scat}, (b) b_{abs}, and (c) b_{ext}. The modeled source b_{scat}, b_{abs}, and b_{ext} were strongly correlated linearly with the measured optical b_{scat} (R^2 = 1.00, slope = 1.00), b_{abs} (R^2 = 0.99, slope = 0.99), and b_{ext} (R^2 = 1.00, slope = 1.00), indicating that the six identified sources can adequately account for the variability in aerosol optical coefficients.
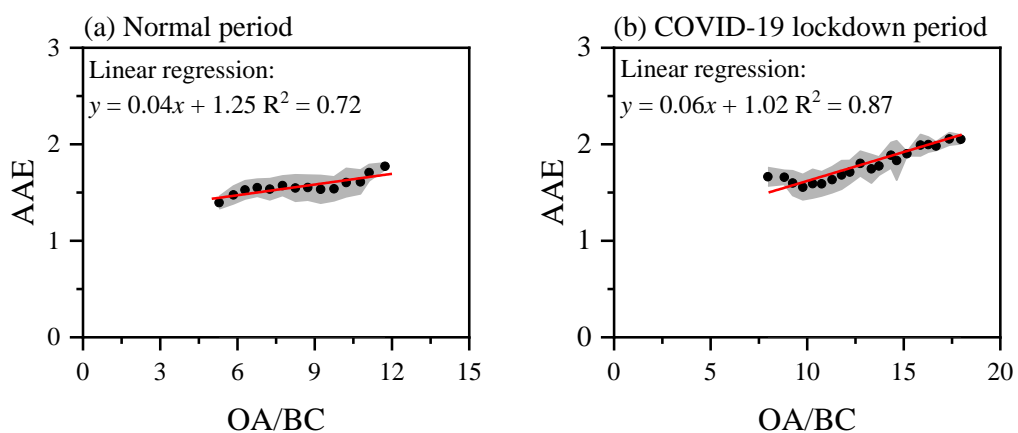
Figure S12. Linear relationships between the AAEs and the mass concentration ratios of organic aerosol (OA) to BC (OA/BC) during the normal (a) and lockdown (b) periods. The intercept of the linear regression represents the realistic AAE_{BC}. The points and light gray shadows represent the mean values and error margins in each bin (Δ(OA/BC) = 0.5).

145 **Table S1.** Summary of chemical and meteorological measurements of in Xi'an before and during the

146 COVID-19 lockdown period.

Parameters	Sampling interval	Instruments and online source	Operation and calibration
Chemical variables			
NO_3^-, SO_4^{2-}, NH_4^+, Cl^-, and OA	15-min	Quadrupole aerosol chemical speciation monitor (Q-ACSM, Aerodyne Research Inc., Billerica, Massachusetts, USA)	The relative ionization efficiencies (RIEs) for OA, nitrate, and chloride were set to 1.4, 1.1, and 1.3 by default, respectively. The RIE for ammonium (5.8) was determined from the ammonium nitrate aerosol calibration, while the RIE for sulfate (1.9) was estimated by fitting the measured sulfate versus predicted sulfate values. The collection efficiency was set to 0.45.
Si, K, Ca, Cr, Mn, Fe, Zn, As, Se, Ba, Hg, and Pb	1-hour	Xact 625 ambient metals monitor (Xact 625i, Cooper Environmental Services, Beaverton, OR, USA)	Daily advanced quality assurance checks were performed during 30 min after midnight to monitor shifts in the calibration.
$PM_{2.5}$ and NO_x	5-min	The Department of Ecology and Environment of Shaanxi Province (http://sthjt.shaanxi.gov.cn, in Chinese)	
Meteorological variables[*]			
WS, WD, T, P, and DP	1-hour	Integrated automatic weather station (MAWS201, Vaisala, Helsinki, Finland)	
PBLH	3-hour	Global Data Assimilation System (ftp://arlftp.arlhq.noaa.gov/pub/archives/gdas1)	PBLH at the sampling site was obtained using linear interpolation method.

147 [*]WS, WD, T, P, DP, and PBLH represent wind speed, wind direction, temperature, pressure, dew point,

148 and planetary boundary layer height, respectively.

149 **Table S2.** Summary of output indices from the constructed b_{ext} GAM.

Intercept	6.64	
Adjusted R^2	0.54	
Smoothed parameters[*]	F value	p value
f(WS)	3.402	0.002331
f(WD)	5.820	0.000134
f(T)	2.707	0.012809
f(P)	3.209	0.001757
f(DP)	13.325	$< 2.00 \times 10^{-16}$
f(PBLH)	3.656	0.026822

150 [*]WS, WD, T, P, DP, and PBLH represent wind speed, wind direction, temperature, pressure, dew point,

151 and planetary boundary layer height, respectively.

152 **Table S3.** Concurvity indices between each independent smoothed parameter in the constructed GAM.

Smoothed parameters[*]	$f(WS)$	$f(WD)$	$f(T)$	$f(P)$	$f(DP)$	$f(PBLH)$
$f(WS)$	1.00	0.28	0.03	0.09	0.07	0.23
$f(WD)$	0.15	1.00	0.08	0.09	0.03	0.07
$f(T)$	0.06	0.07	1.00	0.11	0.25	0.22
$f(P)$	0.08	0.24	0.08	1.00	0.06	0.09
$f(DP)$	0.05	0.06	0.08	0.07	1.00	0.05
$f(PBLH)$	0.13	0.07	0.05	0.04	0.06	1.00

153 [*]WS, WD, T, P, DP, and PBLH represent wind speed, wind direction, temperature, pressure, dew point,

154 and planetary boundary layer height, respectively.

References

Lack, D. A. and Cappa, C. D.: Impact of brown and clear carbon on light absorption enhancement, single scatter albedo and absorption wavelength dependence of black carbon, Atmos. Chem. Phys., 10, 4207–4220, https://doi.org/10.5194/acp-10-4207-2010, 2010.

Lack, D. A. and Langridge, J. M.: On the attribution of black and brown carbon light absorption using the Ångström exponent, Atmos. Chem. Phys., 13, 10535–10543, https://doi.org/10.5194/acp-13-10535-2013, 2013.

Moosmüller, H., Chakrabarty, R. K., Ehlers, K. M., and Arnott, W. P.: Absorption Ångström coefficient, brown carbon, and aerosols: basic concepts, bulk matter, and spherical particles, Atmos. Chem. Phys., 11, 1217–1225, https://doi.org/10.5194/acp-11-1217-2011, 2011.

Norris, G., Duvall, R., Brown, S., and Bai, S.: EPA positive matrix factorization (PMF) 5.0 fundamentals and user guide, 2014.

Rai, P., Furger, M., Slowik, J. G., Canonaco, F., Fröhlich, R., Hüglin, C., Minguillón, M. C., Petterson, K., Baltensperger, U., and Prévôt, A. S. H.: Source apportionment of highly time-resolved elements during a firework episode from a rural freeway site in Switzerland, Atmos. Chem. Phys., 20, 1657–1674, https://doi.org/10.5194/acp-20-1657-2020, 2020.

Yuan, J. F., Huang, X. F., Cao, L. M., Cui, J., Zhu, Q., Huang, C. N., Lan, Z .J., and He, L. Y.: Light absorption of brown carbon aerosol in the PRD region of China, Atmos. Chem. Phys., 16, 1433–1443, https://doi.org/10.5194/acp-16-1433-2016, 2016.